Gravity wave events from mesoscale simulations, compared to polar stratospheric clouds observed from spaceborne lidar over the Antarctic Peninsula

V. Noel, M. Pitts

Gravity wave events from mesoscale simulations, compared to polar stratospheric clouds observed from spaceborne lidar over the Antarctic Peninsula

V. Noel[1] and M. Pitts[2]

Received 12 December 2011; revised 26 April 2012; accepted 29 April 2012; published 6 June 2012.

[1] We compare Gravity Waves (GW) and Polar Stratospheric Clouds (PSC) above the Antarctic Peninsula for winters (June to September) between 2006 and 2010. GW activity is inferred from stratospheric temperature and vertical winds from the Weather and Research Forecast mesoscale model (WRF), and documented as a function of time and geography for the studied period. Significant GW activity affects 36% of days and follows the Peninsula orography closely. Volumes of PSC, composed of ice and Nitric Acid Trihydrate (NAT), are retrieved using observations from the spaceborne lidar CALIOP (Cloud-Aerosol Lidar with Orthogonal Polarization). They are documented against GW activity as a function of time and longitude. Sixty-three percent of ice PSC are observed during GW events, when the average volume of PSC per profile doubles. Maximum ice PSC volumes are seen directly over the Peninsula (65°W), while maximum NAT PSC volumes appear downstream further East (∼35°W). Effects of GW events on NAT PSC are felt as far East as 40°E. Our results support the importance of gravity waves as a major mechanism driving the evolution of ice PSC in the area, but the effects on NAT PSC are harder to detect. After a GW event ends, volumes of ice PSC get back to their usual levels in less than 24 h, while this process takes more than 48 h for NAT PSC. Daily profiles of H_2O and HNO_3 mixing ratios, retrieved from MLS observations, are used to derive ice and NAT frost points with altitude and time. Combining these frost points with modeled stratospheric temperatures, the volumes of air able to support ice and NAT crystals are quantified and compared with PSC volumes. Correlation is high for ice crystals, but not for NAT, consistent with their much slower nucleation mechanisms. Observations of ice PSC over the domain are followed by a strong increase (+50–100%) in NAT PSC formation efficiency 2 to 6 h later. This increase is followed by a steep drop (6–10 h later) and a longer period of slow decline (10–24 h later), at the end of which the NAT PSC formation efficiency is less than half its initial value. The fact that these effects tend to cancel each other out, coupled to the important lag in NAT PSC reaction to GW activity, suggest why it is especially difficult to quantify how GW activity impacts NAT PSC cover.

Citation: Noel, V., and M. Pitts (2012), Gravity wave events from mesoscale simulations, compared to polar stratospheric clouds observed from spaceborne lidar over the Antarctic Peninsula, *J. Geophys. Res.*, *117*, D11207, doi:10.1029/2011JD017318.

1. Introduction

[2] Polar Stratospheric Clouds (PSC) form during polar winter nighttime, May to September in Antarctica. They play an active part in the formation of the seasonal ozone hole, as heterogeneous reactions on PSC particles transform passive species (such as HCl and HBr) into active chlorine and bromine that cause ozone loss [*Solomon*, 1999]. Moreover, during sedimentation PSC particles scavenge nitric acid, slowing down the reconversion of active chlorine into passive species necessary to ozone recovery [*Jensen et al.*, 2002]. Climate-change related drops in stratospheric temperatures could increase PSC formation, leading to enhanced polar ozone depletion [*Hitchcock et al.*, 2009].

[3] The formation of PSC particles is driven by stratospheric temperature, pressure and available mixing ratios of nucleating species. Depending on these factors, nucleation processes lead to the formation of solid NAT (Nitric Acid

[1]Laboratoire de Météorologie Dynamique/IPSL, Ecole Polytechnique, CNRS, Palaiseau, France.
[2]NASA Langley Research Center, Hampton, Virginia, USA.

Corresponding author: V. Noel, Laboratoire de Météorologie Dynamique, Ecole Polytechnique, FR-91128 Palaiseau, France. (vincent.noel@lmd.polytechnique.fr)

0148-0227/12/2011JD017318

Trihydrate, water and HNO_3), liquid STS (Supercooled Ternary Solution, water, HNO_3 and H_2SO_4) or solid ice particles. PSC made of these particles are often described, respectively, as Type Ia, Ib and II (roughly from the most to least frequent). This classification originates in the existence of PSC families with distinct optical properties as seen from lidar [*Poole and McCormick*, 1988]. Uniquely matching those properties to chemical composition is hard as PSC often contain a mixture of all particle types, but it is often convenient to describe a PSC whose composition is dominated by a given particle type. Secondary particle types have been described, e.g., Enhanced NAT [*Tsias et al.*, 1999] or NAT rock [*Fueglistaler et al.*, 2002], but are more rare.

[4] Temperature is the main factor driving the extent and composition of PSC cover. It needs to be colder than specific thresholds for ice, NAT or STS formation, depending on the abundance of source species [*Höpfner et al.*, 2009]. At average levels of stratospheric water vapor and HNO_3, the sustained existence of ice particles requires temperatures colder than ~192 K at 100 hPa and ~183 K at 20 hPa [*Marti and Mauersberger*, 1993], while the NAT threshold is 6–7 K warmer [*Hanson and Mauersberger*, 1988]. Particle nucleation generally requires some supersaturation, which for equivalent mixing ratios requires temperatures ~3 K colder [*Koop et al.*, 2000]. In the Arctic, stratospheric temperatures generally hover around those thresholds [*Pitts et al.*, 2011], and external processes acting on temperatures are crucial in driving the presence and eventual cover of PSC. In the Antarctic, during most of the polar winter stratospheric temperatures are generally colder than required for PSC formation. External processes still play a role, especially during the early, warmer stages of polar winter (i.e., May–June [*McDonald et al.*, 2009]) but also later into the season, depending on atmospheric conditions. Gravity waves (GW) are among the most important of such mechanisms: they generate intense temperature fluctuations that propagate up to the mid-stratosphere [*Plougonven et al.*, 2008], where they lead to the accelerated formation of PSC [*Alexander et al.*, 2009; *Innis and Klekociuk*, 2006; *Kohma and Sato*, 2011]. The Antarctic Peninsula is noticeable for its intense GW activity [*Alexander and Teitelbaum*, 2007], but GW happen in all wintertime polar areas [*Baumgaertner and McDonald*, 2007].

[5] The spaceborne lidar CALIOP (Cloud-Aerosol Lidar with Orthogonal Polarization) on the CALIPSO satellite (Cloud Aerosol Lidar and Infrared Pathfinder Satellite Observation) monitors Earth continuously and autonomously since 2006 [*Winker et al.*, 2007]. CALIOP's high sensitivity to weakly opaque atmospheric features, and its ability to document their vertical variability, allows a very accurate retrieval of the location and altitude of optically thin clouds [*Martins et al.*, 2011], among them PSC. CALIOP's sensitivity to light polarization allows the identification of PSC types [*Pitts et al.*, 2007], while its frequent overpasses of polar regions (~14 times a day) insures the sampled PSC are representative of the cloud cover. Thanks to these advantages, CALIOP observations have led to breakthrough insights into PSC properties and processes, and provided a comprehensive overview of the seasonal evolution of PSC population across several years over Antarctica [*Noel et al.*, 2008; *Pitts et al.*, 2009].

[6] In a previous paper, we described an optically thick ice PSC observed by CALIOP during at least 2 days over the Antarctic Peninsula [*Noel et al.*, 2009]. High-resolution mesoscale simulations showed it formed following intense, quasi-stationary temperature drops (~15 K) linked to orographic gravity waves. These brought stratospheric temperatures well below the ice frost point, leading to the fast generation of ice crystals. Nearby observations revealed a NAT PSC downstream with respect to the polar vortex, while upstream was clear-sky. Back-trajectories confirmed that the air masses holding the NAT PSC went through the GW-affected area. This suggests NAT crystals nucleated on sublimating ice particles sedimenting from the GW-generated ice PSC and advected by the strong winds of the polar vortex, a process known as mountain-wave seeding, first identified by *Carslaw et al.* [1998] and documented over the Peninsula by *Höpfner et al.* [2006]. The details of this process, its generality and importance for the general PSC population over Antarctica, remain poorly known and hard to quantify.

[7] Here several years of data are used to investigate how GW over the Antarctic Peninsula influence ice and NAT PSC. First, atmospheric properties from a mesoscale model document stratospheric GW activity during south hemisphere winters between 2006 and 2010 (section 2). CALIOP observations then document volumes of ice and NAT PSC during the same period (section 3), which are interpreted against GW activity from the previous section. Finally, model output are combined with observations of PSC and mixing ratios, to document the effect of GW activity on PSC formation efficiency from the intersecting data set (section 4). Results are summarized and discussed in section 5.

2. Gravity Wave Activity

2.1. Model Setup

[8] The Weather Research and Forecast model [*Skamarock et al.*, 2005], WRF v. 3.2.1, ran on a 100 × 100 grid cells domain centered on the Peninsula, with 20 km horizontal resolution and 120 vertical levels. Minimum pressure was requested as 5 hPa with a 3 km damping layer to avoid reflections of atmospheric waves on the domain lid. Topography was derived from the database provided with WRF. 38 vertical levels were available in the 120–10 hPa vertical range where PSC are most frequent. Initial and boundary conditions for the model were provided by 6-hourly ERA-Interim reanalyses at 0.75° resolution [*Simmons et al.*, 2006]. Stratospheric state was saved every 3 h. Simulations were run along consecutive 4-days periods, overlapping by one day. The first day of each period was discarded as warm-up. Simulations cover June 1st to September 30th, between 2007 and 2010. For 2006 simulations began June 14th (i.e., when CALIOP observations start). In the output, only the center 90 × 90 cells (1800 × 1800 km) were considered to avoid border effects.

2.2. A Gravity Wave Event: July 17th, 2006

[9] Gravity Waves lead to intense spatial fluctuations of vertical wind. Figure 1 shows its maximum variation along the vertical between 120 and 10 hPa, from the WRF output for July 17th, 2006 at 12:00UTC. This is roughly the peak

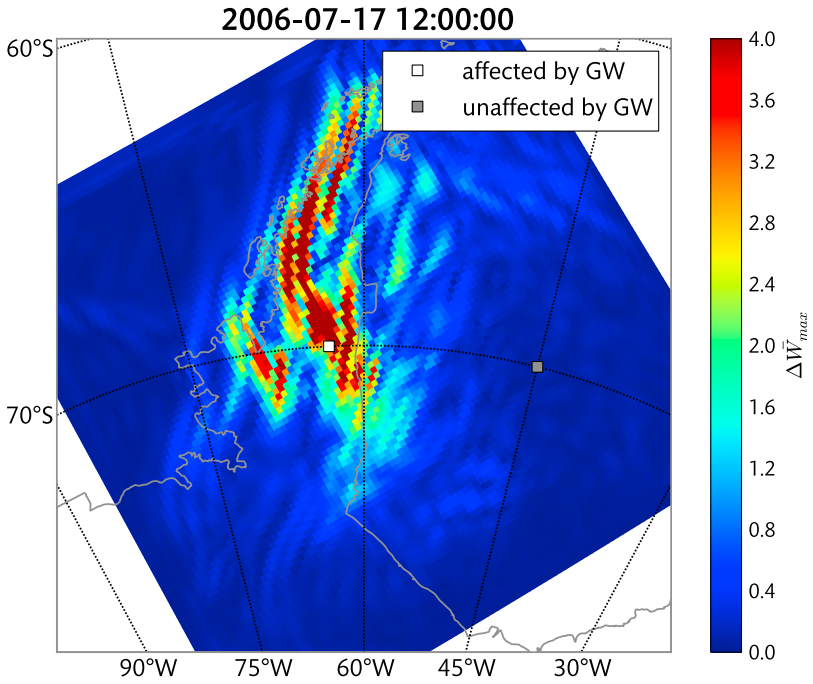

Figure 1. Map of the geographic distribution of the maximum variation of vertical wind speed (m/s) across the vertical dimension of the simulated domain (10–120 hPa) on July 17th, 2006 at 12:00UTC. Coordinates for the domain corners are 85.1°W, 64.9°S (top left), 54.4°W, 59.5°S (top right), 27.3°W, 69.7°S (bottom right) and 76.9°W, 80.4°S (bottom left).

activity during a GW event (chosen randomly in the data set) that began on July 16th near 12:00UTC, when wind and temperature fluctuations appeared in simulated fields above the Peninsula (~65°W). The event lasted until July 20th, when fluctuations disappeared near 06:00UTC.

[10] Large variations in vertical wind are calculated directly above the Peninsula, North of 74°S between 73°W and 55°W. Profiles of vertical wind speed and temperature (Figure 2) were extracted at the white (63°W, 70°S) and gray (45°W, 70°S) spots in Figure 1, respectively strongly affected and unaffected by the GW event. In the GW-affected area (blue lines), vertical winds (Figure 2, left) go from strongly positive (upward motions) to strongly negative (downward motions), and often get faster than 1 m/s.

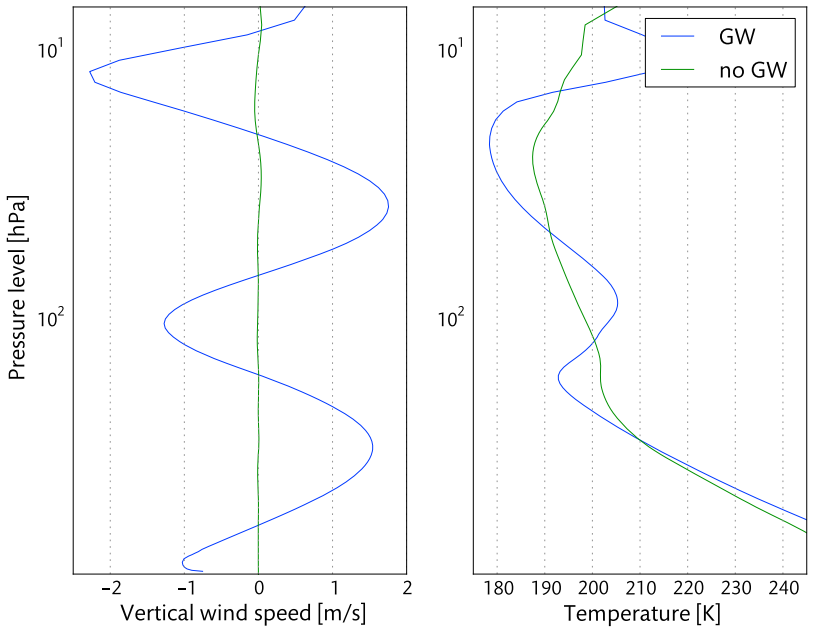

Figure 2. Vertical profiles of (left) vertical wind speed w (m/s) and (right) temperature (K) for the two points identified as being affected by intense (blue line) or no GW activity (green line) in Figure 1.

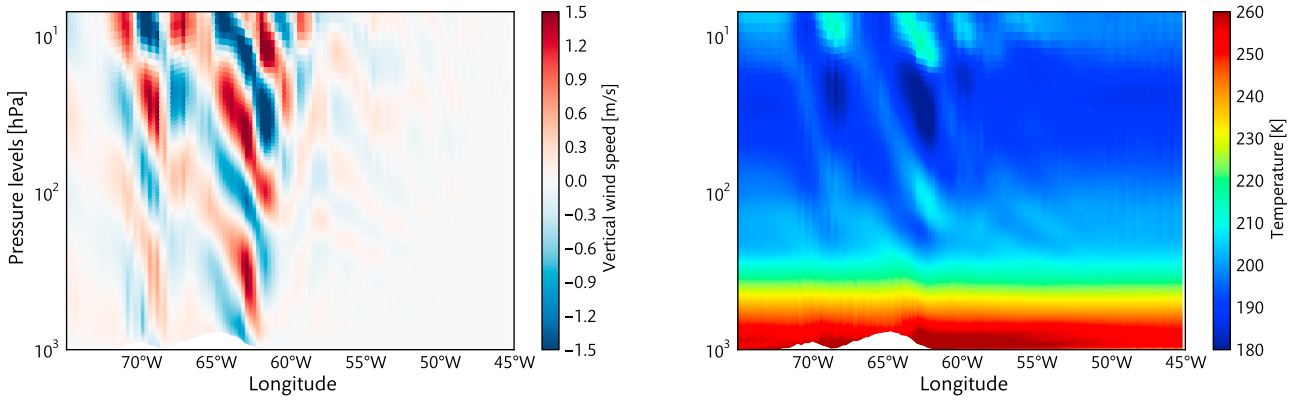

Figure 3. Vertical, zonal cross-sections of (left) vertical wind speed (m/s) and (right) temperature (K) as a function of longitude and pressure for latitude near 70°S on July 17th, 2006 at 12:00UTC.

Associated temperature fluctuations of roughly ±10 K (Figure 2, right) cool air to 180 K at 40 hPa, considerably colder than required for ice crystal formation at such pressure levels (~186 K). In the unaffected area (green lines), vertical motions are slower than 0.05 m/s (Figure 2, left), thus almost negligible, while temperatures get close to the frost point (near ~30 hPa) but do not cross it (Figure 2, right). This shows the importance of GW as triggers of ice PSC formation. As an aside, note how the thermal tropopause inversion (Figure 2 (right), near 130 hPa) is negligible compared to the temperature fluctuations created by the gravity waves (blue line).

[11] Figure 3 presents zonal cross-sections of stratospheric vertical winds (left) and temperature (right) as a function of longitude and pressure, for latitudes near 70°S. Orography is faintly visible in white at the bottom. Strong perturbations in the vertical wind are visible above the East front of two Peninsula peaks (downstream with respect to the polar vortex): the Douglas Range (70°W) and Mount Jackson (65–63°W). This alignment confirms the orographic origin of GW. Atmospheric waves follow the orientation of the vortex and propagate East; their influence is felt as far as 45°W. Looking back at the start of the event (July 16th, not shown), it took roughly 24 h for the waves to extend that far East from 65°W. Vertically, waves affect the entire column up to 10 hPa. Temperature fluctuations (Figure 3, right) are less visually dramatic since their stratified decrease with altitude dominates the figure, but obviously overlap wind fluctuations.

[12] Based on this case and numerous others, GW-affected domain cells were identified as vertical winds faster than 1 m/s between 10 and 120 hPa. Attempts were made to filter out non-GW perturbations based on their typical spatial frequencies through Fourier transforms, but these did not improve the results and were not pursued further.

2.3. GW Frequency Maps

[13] Figure 4 shows how frequently horizontal domain cells are GW-affected during Antarctic winters (June to September) between 2006 and 2010, applying the above criteria based on vertical wind fluctuations on the entire model output. The geographical distribution of GW-affected cells looks similar to the case study (Figure 1), but follows the Peninsula even more closely. Frequencies reach 25% directly above the tallest mountains, consistent with their orographic origin. The shape of affected areas is similar for all months (not shown), although areas which are GW-affected more than 25% of the time are larger in July and smaller in August and September. A second, smaller local maximum of GW frequencies is slightly visible on Figure 4 near mountain peaks at 70°W (probably Mt. Stephenson in the Douglas Range, as in Figure 3). This mountain leads to more GW activity during July (not shown). GW activity is most intense in 2006 and 2010, and weakest in 2007 and 2009.

[14] Figure 5 shows the monthly frequencies of cells affected by GW within 5° longitude bins. GW activity is maximum in July (up to 11% of cells affected), then September and June (8–10%), and minimum in August (up to 6%). In all months GW activity peaks near 65°W, right above the Peninsula mountains. It decreases rapidly eastward and westward, and is almost negligible outside of the 75°W–55°W longitude range. The secondary local maximum observed on the frequency map (Figure 4), west of the Peninsula, also shows up here (thin green line, near 70°W). It is especially visible in July.

2.4. Vertical Wind and Temperature Distributions

[15] Figure 6 shows histograms of speed for vertical winds faster than 1m/s above the simulated domain, between 10 and 120 hPa, every 3 h. The height of peaks describes the fastest wind on a given date, while the colors inform on the number of domain cells affected by winds faster than 1m/s - i.e., the geographical extent of the GW-affected area at a given time. For instance, in 2006, GW were felt during more than 14 consecutive days (June 24th to July 8th), with wind speeds faster than 6 m/s. The optically thick, GW-induced ice PSC described in *Noel et al.* [2009] happens in this period. Small peaks are sporadically observed, for instance during the second half of August 2006. They barely cross the 1m/s threshold and generally last for less than a day. GW activity appears distributed homogeneously across months, even in September.

[16] Figure 7 shows histograms of temperature. Through the winter, temperatures warmer than 220 K disappear during June and come back between mid-August (in 2010) and mid-September (2009). Temperatures are much warmer in September, often above 220 K. Fast vertical winds (Figure 6)

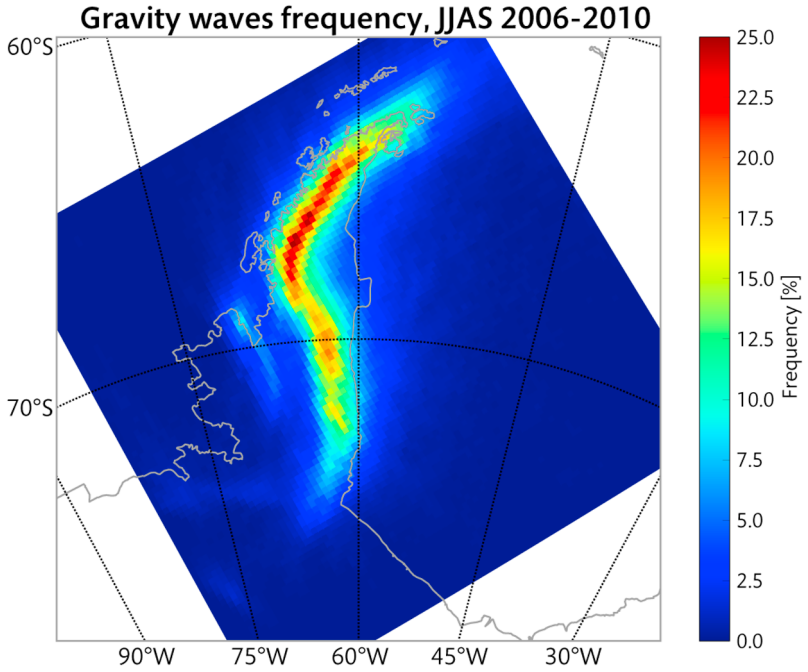

Figure 4. Frequency of domain grid cells being affected by GW events during June–July–August–September 2006–2010.

are often accompanied by roughly symmetrical temperature drops and increases (caused by vertical fluctuations as in Figure 3b). For instance, the 2006 period of uninterrupted GW activity (June 24th–July 8th) reaches temperatures as cold as 160 K. Such an impressive cooling (∼20 K) is however rare, roughly once per winter. Wind and temperatures are not always correlated: for instance, the fast, short-lived vertical winds on August 2nd, 2007 or the last fortnight of August 2008 (Figure 6) are not linked to noticeable temperature drops (Figure 7). It can be hypothesized that, during such events, winds are not strong or widespread enough to generate significant wave activity and temperature drops. To avoid taking those into account, in the rest of the article a GW event is defined as an uninterrupted period of at least 24 h during which at least 10000 km^2 of the domain are GW-affected. As in the previous section, a 400 km^2 cell is considered GW-affected when its vertical winds reach 1m/s.

[17] Table 1 describes GW events identified during Antarctic winters 2006–2010. Out of 587 simulated days, 209 are GW events (36%). 2006 presents a rather small

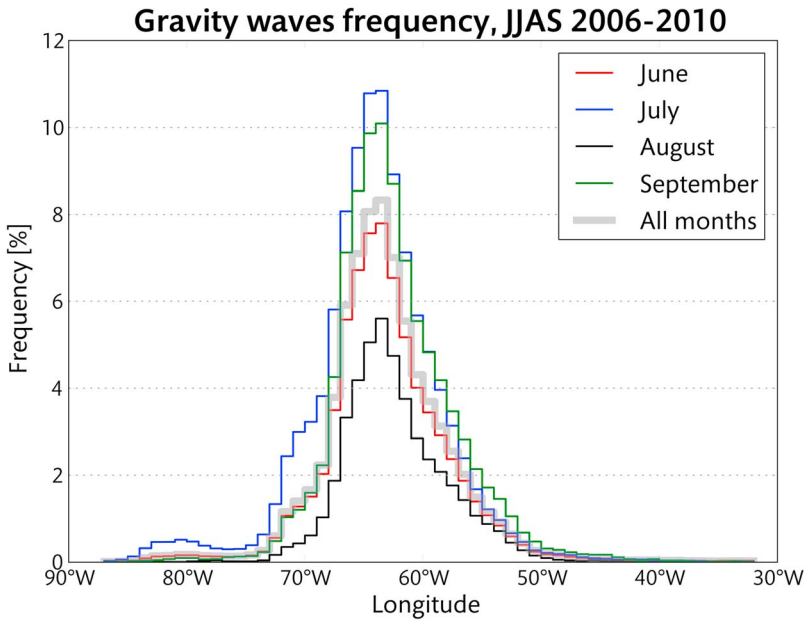

Figure 5. Frequency of GW affecting cell domains as a function of longitude.

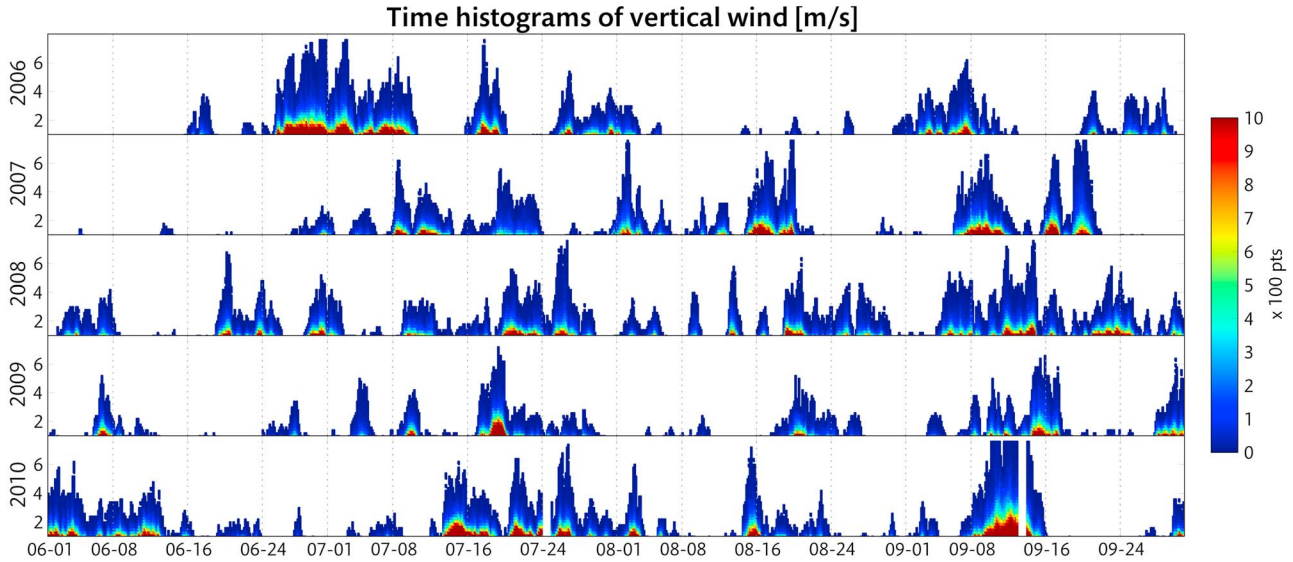

Figure 6. Distributions of absolute vertical wind speeds faster than 1 m/s above the simulation domain (10–120 hPa) as a function of time, for each Antarctic summer between 2006 and 2010. Note that no simulation was run before June 13, 2006 (date of first available CALIOP data).

number of GW events (5) compared to the other years, but includes the longest event (15 days) reaching the fastest vertical winds (10.7 m/s), and the largest volume with fast vertical winds during events (4.0%). On the opposite side of the spectrum, 2008 presents a large number of events (11), spanning the longest period (62 days, 52% of the season). However, these events are short, weak, and affect a small part of the domain (1.1 to 3.4%). As a result, 2008 presents the smallest volume with fast vertical winds during GW events (2%). 2009 has the least GW activity: 25 days in total, or 27% of the season. Among the 209 days of GW events, 29 fall in June, 64 in July, 38 in August and 52 in September, following the same monthly hierarchy of GW activity found in Figure 5. In 3 years out of 5, GW events with the largest affected domain happen in September.

2.5. Comparison With Radiosounding Temperatures

[18] To evaluate the accuracy of the WRF model temperatures, we compared them with data from radiosonde probes [*Connolley and King*, 1993] from the Rothera Research Station (67°S, 68°W) on the Antarctic Peninsula, obtained through the British Antarctic Survey program (as in *Moffat-Griffin et al.* [2011]). During the June to September period, several radiosonde were launched per week, 179 in total in JJAS 2008–2010, documenting stratospheric properties as high as 30 km. Files before 2008 did not include probe coordinates and were not used for the comparison. For each radiosounding, we extracted temperature from the WRF output grid point closest in time and space to each measurement point, imposing a minimum time difference of 1 h and a minimum distance of 0.1° between measurement

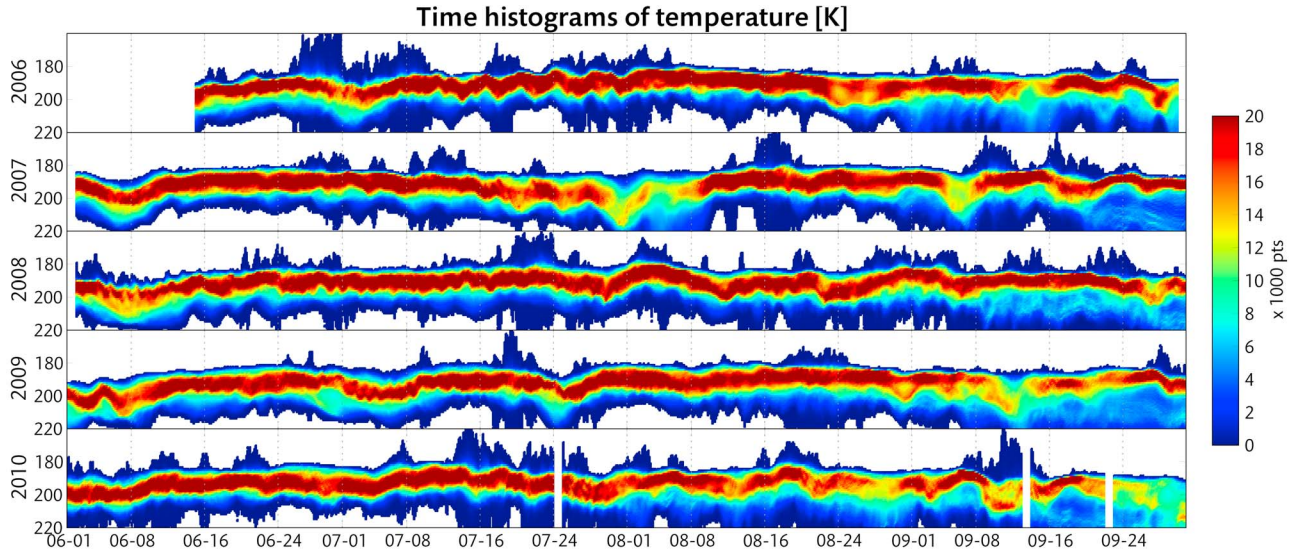

Figure 7. Same as Figure 6, for temperature (K) instead of wind speed.

Table 1. Description of Gravity Wave (GW) Events Identified During Each Antarctic Winter Season Between 2006 and 2010[a]

	GW Event Dates (Length in Days)	Affected Domain (%)	Max Vertical Wind Speed (m/s)	Total Days During Events	Average Affected Domain During Events
2006	6–25 - 7–10 (15)	**5.9**	**10.7**	36 (30%)	4.0%
	7–16 - 7–20 (4)	4	7.8		
	7–25 - 8–03 (8)	2.2	5.2		
	9–02 - 9–09 (7)	2.6	6.1		
	9–20 - 9–22 (2)	2.0	3.9		
2007	7–08 - 7–14 (6)	3.4	6.2	35 (29%)	3.2%
	7–19 - 7–23 (4)	1.3	5.6		
	7–31 - 8–04 (5)	2.4	**9.5**		
	8–11 - 8–13 (2)	1.9	3.2		
	8–15 - 8–21 (6)	3.8	9.3		
	9–06 - 9–12 (6)	**4.7**	6.5		
	9–15 - 9–21 (6)	3.6	7.9		
2008	6–03 - 6–08 (5)	1.3	4.1	62 (52%)	2.3%
	6–19 - 6–26 (7)	1.9	6.6		
	6–28 - 7–02 (4)	2.7	5.2		
	7–09 - 7–13 (4)	1.9	3.5		
	7–19 - 7–29 (10)	2.8	**7.8**		
	8–02 - 8–05 (3)	1.1	3.5		
	8–19 - 8–26 (7)	2.1	6.3		
	8–27 - 8–30 (3)	1.5	3.5		
	9–04 - 9–15 (11)	2.8	7.7		
	9–16 - 9–18 (2)	1.4	4.1		
	9–20 - 9–26 (6)	**3.4**	5.6		
2009	6–06 - 6–09 (3)	2.3	5.1	23 (16%)	2.7%
	7–17 - 7–24 (7)	**3.5**	**7.1**		
	8–19 - 8–24 (5)	1.9	5.0		
	9–09 - 9–17 (8)	2.7	6.4		
2010	6–01 - 6–13 (12)	2.6	6.2	47 (39%)	3.6%
	7–13 - 7–19 (6)	**5.7**	6.0		
	7–20 - 7–31 (11)	3.4	7.3		
	8–02 - 8–03 (1)	3.9	5.9		
	8–14 - 8–20 (6)	1.8	7.1		
	8–21 - 8–23 (2)	0.8	4.1		
	9–02 - 9–04 (2)	0.7	3.0		
	9–07 - 9–16 (7)	**6.0**	**10.2**		

[a]Given are dates (m–dd), percentage of domain affected by fast vertical winds, maximum vertical wind speed (m/s), total number of days affected by GW events for each year (and percentage of simulated season), and average percentage of domain affected by fast vertical winds for each year. Within individual years, the largest affected domain and fastest maximum vertical wind speed are boldface.

and model grid point. This limited the number of available measurements above the 120 hPa level, as the probes were more susceptible to leave the modeled domain as they reached higher altitudes.

[19] Comparisons conducted over all radiosoundings in JJAS 2008–2010 show that over all years and pressure levels, modeled WRF temperatures are warmer by +0.4 K (±2.9 K) compared to radiosonde measurements. For the pressure levels between 10 and 120 hPa considered here, this warm bias increases to 1.3 K (±2.5 K). Year averages change less than 0.1 K from one year to the next, but month averages increase during the winter season, from 1.1 K in June to 1.7 K in September. Using high-resolution probe data showed that this bias also increases with altitude, from less than 1 K near 100 hPa to almost 4 K near 10 hPa. This warm bias is not affected by GW activity (as given by Table 1), suggesting that the impact of GW on stratospheric activity is reproduced well by the model. This warm bias is well above the uncertainty of the RS92 probes (0.15 K [*Steinbrecht et al.*, 2008]) used at Rothera from 2007 on. We plan to identify its source in a future study.

3. GW Events and PSC Observations

3.1. PSC Observations From CALIOP

[20] As in *Noel et al.* [2008] and 2009, PSC were detected in CALIOP observations of total attenuated backscatter (TAB) through the following steps: (1) averaging TAB profiles horizontally over 10 km to improve the signal-to-noise ratio, (2) thresholding the TAB above the molecular backscatter (normalized in PSC-free regions between 34 and 38 km of altitude) to retrieve PSC altitudes, (3) removing spurious detections due to nongeophysical signal fluctuations, by imposing specific geometries typical of PSC, such as minimal horizontal and vertical extensions. In addition to previous efforts, we added an extra step of threshold-based detection from perpendicular backscatter, as in *Pitts et al.* [2009]. Ice and NAT classification was based on layer-integrated depolarization and scattering ratios, following the boundaries in *Pitts et al.* [2009]. For simplification, a single class of NAT was considered, in contrast with *Pitts et al.* [2009, 2011] who considered respectively two and three NAT classes. From these retrievals, we calculated volumes of air containing NAT and ice PSC, hereafter called NAT and ice PSC volumes. We supposed a CALIOP point describes a three-dimensional section of atmosphere, defined by CALIOP's vertical resolution (60 to 300 m depending on altitude) and the horizontal footprint of profiles. To simplify the comparison with simulations (section 2), this footprint was supposed rectangular with dimensions defined by the horizontal averaging used here (10 km × 10 km). A volume was thus calculated for each CALIOP point identified as NAT or ice PSC; PSC volumes were then summed and binned along time and space coordinates for analysis purposes.

[21] PSC retrieval and classification using the present algorithm were compared with the data set from *Pitts et al.* [2011] (hereafter called NASA data set) for August 2007 over the domain defined in section 2.1 (not shown). In contrast with the present detection, which considers a single horizontal averaging distance of 10 km, cloud detections in the NASA data set are based on a multiresolution horizontal averaging scheme (5, 15, 45 and 135 km). The present data set agrees well with the NASA one for a 15 km horizontal averaging distances, consistent with the 10-km averaging resolution selected here. For such detections, the difference between data sets in average daily PSC volume per profile (considering all PSC types) is less than 1%. This variation is also less than 1% considering only PSC classified as NAT and less than 4% considering only PSC classified as ice in both data sets. Including PSC detected at a 135 km averaging distance in the NASA data set increases the total PSC volume by a few percent. These percent contain the optically thinnest PSC, requiring the largest averaging for detection: primarily young STS PSC emerging from sulfate aerosols, or NAT PSC with low number densities. Overall, the present data set contains slightly fewer PSC than the NASA data set considering all averaging resolutions. Since the present article studies ice and NAT PSC, an accurate detection of optically thinner STS PSC was not attempted (as in the more comprehensive NASA data set) and lower detection rates on

Table 2. Average Daily PSC Volume per Profile (km^3) Observed by CALIOP Over the Domain Defined in Section 3.1, for Ice and NAT PSC, for Each Year Between 2006 and 2010 and Each Month[a]

	Average Ice PSC Volume per Profile (km^3)	Average NAT PSC Volume per Profile (km^3)
2006	4.2	**51.3**
2007	3.7	36.7
2008	**6.2**	46.4
2009	2.6	28.8
2010	3.9	22.7
June	0.8	25.1
July	6.0	**78.4**
August	**6.7**	30.3
September	3.2	11.3

[a]Maximum volumes are boldface.

these clouds should be expected. For the present purposes of analyzing ice and NAT PSC, we consider the difference between both data sets to be small enough for them to be statistically equivalent.

3.2. PSC Detections and Volumes

[22] PSC Observations were analyzed between 60°S and 70°S, for consistency with the analysis of *Alexander et al.* [2011], and between 100°W and 100°E, to cover the influence zone of Peninsula gravity waves. Due to its limited horizontal field of view, CALIOP observes less than 25% of this domain each day; moreover, this sampling is irregular, i.e., the number of CALIOP profiles in the domain changes from one day to the next. To account for this imperfect sampling, PSC volumes are normalized by the number of available CALIOP profiles in the studied region over the time period of aggregation. Hence we present PSC volumes per profile, which should be independent of sampling fluctuations. For the sake of brevity, these will be referred to simply as PSC volumes from now on. Days with less than 500 profiles were discarded for fear they would bias results.

[23] Over the 2006–2010 Antarctic winters (JJA), 553 days over 587 were considered adequately sampled (∼94%). Ice PSC appear in 34% of them (i.e., an ice PSC was identified in at least one CALIOP profile). GW events contain 191 well-sampled days, 46% of which showed ice PSC presence. Calm periods contain 124 well-sampled days with ice PSC 19% of the time. NAT PSC were almost ubiquitous as they were detected 92% of the time, with no difference between GW events or calm periods. Thus, in this domain, ice PSC are more frequent than average during GW events; this is not true for NAT PSC. Overall, 63% of ice PSC and 46% of NAT PSC volume were observed during GW events, while GW events affected only 36% of days. Average volumes are 4.1 km^3 per profile for ice PSC and 36.4 km^3 for NAT PSC (roughly 10 times larger). This very large difference is mostly due to ice PSC being much less frequent than NAT PSC, a large number of unaffected profiles are thus counted in the average. Section 3.4 will show that this difference decreases significantly when only cloudy periods are considered. The largest average volumes of ice and NAT PSC (Table 2) are observed in 2008 (which had the most days affected by GW events, Table 1) and 2006 (which had the longest and most intense GW events). The smallest volume is observed in 2009 for ice PSC (which had the minimum GW activity) and 2010 for NAT PSC. These results suggest that, first and foremost, the intensity of GW activity directly affects the observed volume of PSC in the domain. Second, long and intense GW events are correlated with more NAT PSC, and short and numerous events with more ice PSC. Considering monthly averages, ice PSC volumes increase from June to reach their maximum in August, following the seasonal evolution of background stratospheric temperatures and the trend in GW events found in Figure 5 and section 2.4. This supports the idea that GW activity is most important for PSC formation when background temperatures are already close to the frost point [*McDonald et al.*, 2009]. September volumes (3.2 km^3) are halved compared to August (6.7 km^3), but are still large compared to June levels (0.8 km^3). This number can be understood as a compromise reached through the combined effect of an intense GW activity with the overall warmer September temperatures. NAT PSC volumes reach their maximum earlier, in July (75.6 km^3), and it is triple the June and August volumes (24.2 and 24.2 km^3). Their minimum extent is reached in September (11.2 km^3).

3.3. PSC Volumes During Antarctic Winters (2006–2010)

[24] Figure 8 shows how daily PSC volumes change during five Antarctic winter seasons in the considered domain. GW events (thick lines) do not necessarily produce ice or NAT PSC. For example, the extended 2006 GW event (June 25th to July 10th) contains two spikes in ice PSC volume (June 28th and July 8th), but these are separated by 7 days without ice PSC. A local maximum of NAT PSC is observed close to the beginning of the event (June 28th), but the following drop in NAT PSC volume (until July 3rd) also happens during the GW event. This specific GW event therefore includes both increases and decreases in ice and NAT PSC volumes.

[25] It is worth noticing again the limited ice and NAT PSC volume during 2009 compared to 2006 and 2008. 2009 is the year of minimum GW activity and shows the warmest stratospheric background (195.4 K on average between 10 hPa and 120 hPa) compared to 2006 and 2008 (194 K), years of intense GW activity. Moreover, ice and NAT PSC volumes are more stable during periods without GW - this is especially noticeable by comparing 2009 with other years, or focusing on August 2006 and 2008. It suggests that GW events are linked to fluctuations in PSC volume. Second, all significant increases in ice PSC volumes happen during GW events, except two (July 24th, 2006 and July 4th 2009). Outside GW events, ice PSC formation happens only rarely, and ice PSC volumes are often decreasing to zero. NAT PSC, on the other hand, are often observed out of GW events - e.g., June–July 2009. GW events thus appear to trigger ice PSC formation, and do it more efficiently when the background temperature is colder. Finally, ice PSC increases seem correlated with simultaneous, or slightly delayed, increases in NAT PSC volume. This is however not specific to GW events, see e.g., ice PSC volumes increase on July 4th, 2009 and NAT PSC follow the next day.

[26] These remarks do not apply to every case, but CALIOP's sampling of the domain is imperfect: on a given

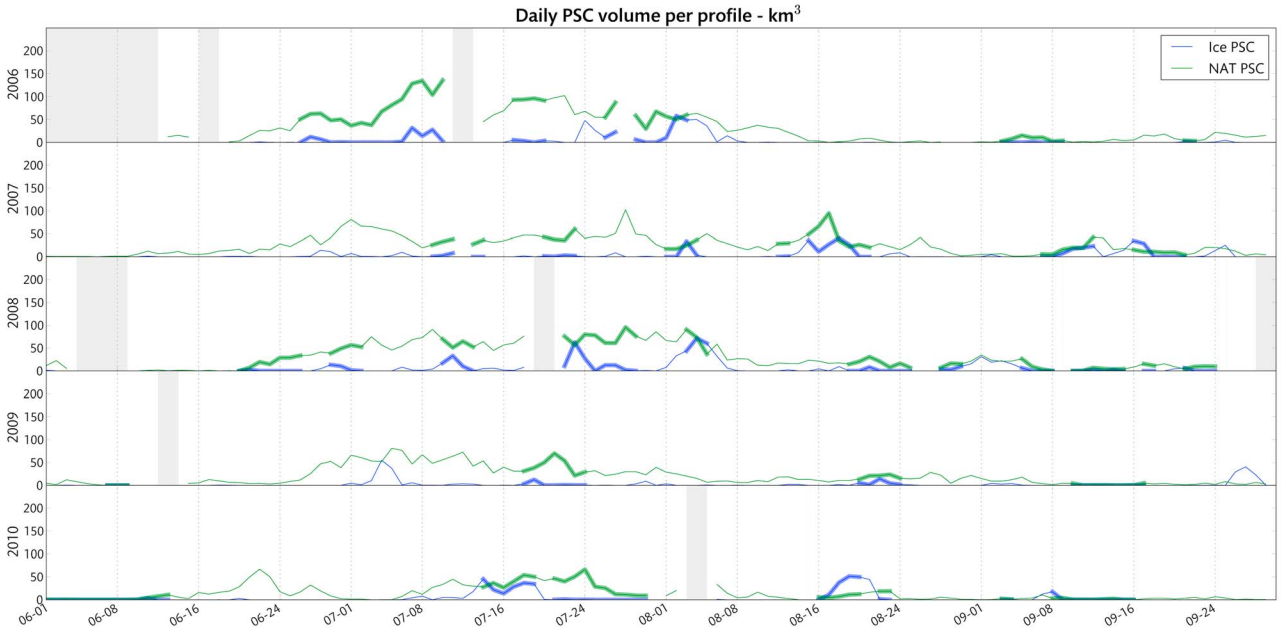

Figure 8. Evolution of PSC volume per profile along each Antarctic winter between 2006 and 2010, for ice (blue) and NAT (green) PSC. Thick lines indicate periods identified as GW events following Table 1. Shaded regions indicate undersampled periods (e.g., missing CALIOP observations).

day a NAT PSC can be observed and the nearby ice PSC missed, or vice versa. This could be mitigated by using longer averaging times, but then the slight delay in NAT PSC increase would be missed.

3.4. Distribution of Daily PSC Volumes

[27] Figure 9 shows the distribution of daily averaged PSC volume, considering the whole observation period (2006–2010). Only days with PSC observations were considered,

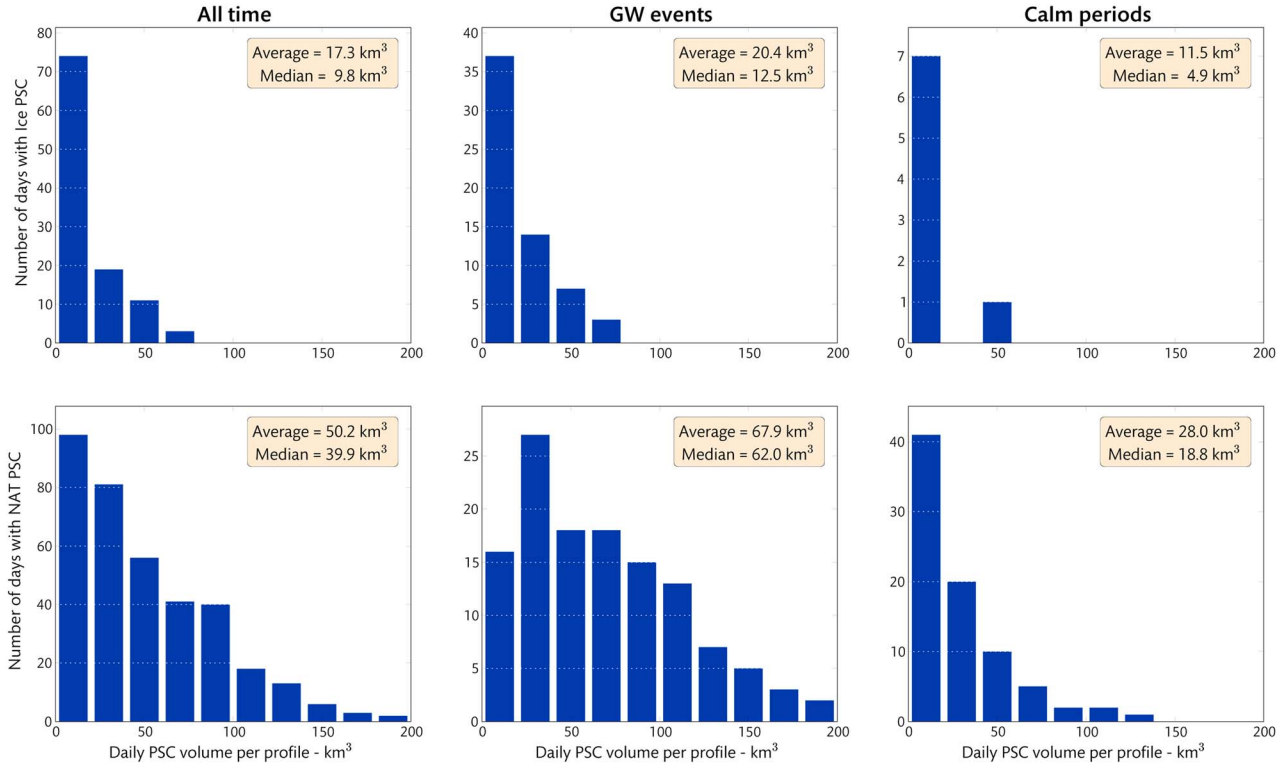

Figure 9. Distribution of daily PSC volume per profile for PSC identified as (top) ice and (bottom) NAT, (left) for all seasons, (middle) during GW events and (right) during calm periods.

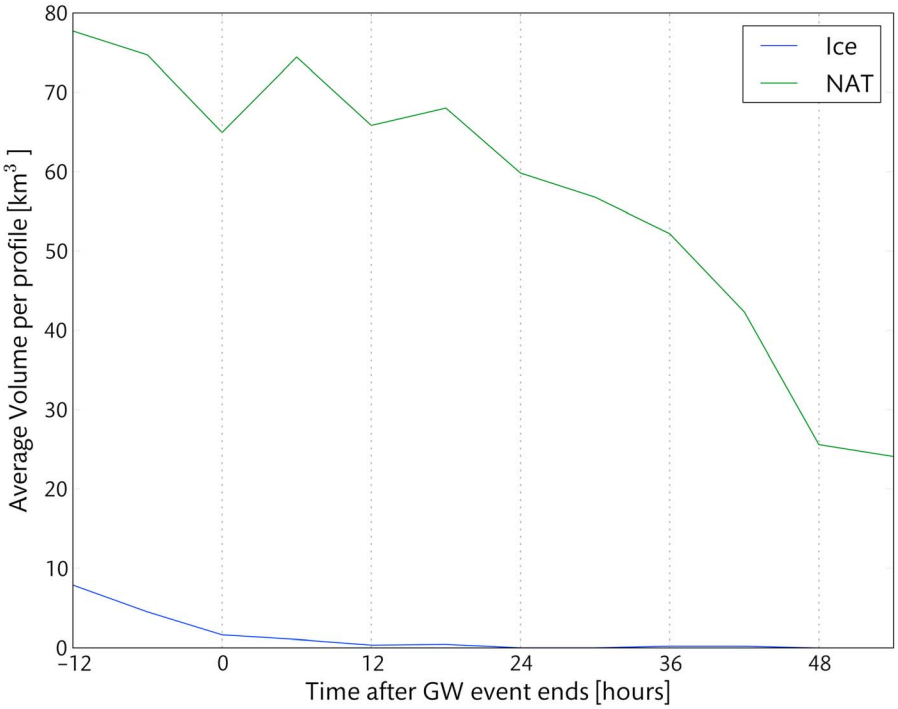

Figure 10. Evolution of the volume per profile of ice and NAT PSC as a function of time after the end of GW events.

i.e., 34% of days for ice PSC and 92% of days for NAT PSC (section 3.2) - in other words, the most frequent daily volume of ice PSC is 0 km^3, but is not shown in the distributions. All days are included in the left column, GW events (from Table 1) in the middle, and calm periods on the right, for ice (Figure 9, top) and NAT (Figure 9, bottom) PSC. Calm periods are defined as limited GW activity for at least 48 h straight, occurring at least 24 h after the end of a GW period, to let GW-related effects dissipate. Limited GW activity is defined as less than 2000 GW-affected km^2 in the domain.

[28] PSC volumes are roughly 4 times larger for NAT than ice. Daily PSC volumes stay below 100 km^3 per profile for ice and 200 km^3 per profile for NAT. In calm periods, ice PSC volumes are small: 11 km^3 per profile on average, with a 4.9 km^3 median. The median might be more significant, as a single day with ice PSC volume of 45 km^3 skews the mean (Figure 9, top right). During GW events, ice PSC volumes are large: 20.4 km^3 on average, with a 12.5 km^3 median (roughly twice the one in calm periods). Volumes larger than 50 km^3 begin to appear. NAT PSC volumes are also considerably larger during GW events: 67.9 km^3 on average, more than twice the average of calm periods (28.0 km^3). NAT volumes larger than 200 km^3 are frequent in GW events. These results show a strong impact of GW events on PSC volumes.

3.5. PSC Volumes as a Function of Time

[29] We extracted ice and NAT PSC volumes in CALIOP observations as a function of time after the end of each GW-affected period (Table 1) followed by at least 48 GW-free hours. Along these 48 h, PSC volumes (Figure 10) transition between the averages for GW events and calm periods (Figure 9). The transition takes a different time for each PSC type. The ice PSC volume (blue line in Figure 10) drops down quickly, taking 12 to 24 h to get back to the near-zero volumes found in GW-free periods. The fastest decline in ice PSC volume is right after GW events end. NAT PSC volumes (green line) stay affected much longer, taking as long as 48 h to drop down to the 20–30 km^3 level typical of volumes observed during calm periods. The steepest decline in NAT PSC volumes occurs between hours 36 and 48, when a ∼50% drop is recorded.

3.6. PSC Volumes as a Function of Longitude

[30] Figure 11 shows ice and NAT PSC volumes as a function of longitude in 10° bins. During GW events (Figure 11, top), ice PSC volume (blue line) is maximum near 75°W (∼75 km^3), right above the GW-triggering orography of the Peninsula. Large volumes (>25 km^3) extend far sideways (80°W–30°W), especially East. Outside of this longitude range, the volume of ice PSC is smaller, down to levels observed during calm periods. Thus the very small ice PSC volume reported in section 3.2 (4.1 km^3 per profile) is explained by (1) the rarity of ice PSC in time (sections 3.2 and 3.3), and (2) their acute geographic locality. However, ice PSC reach large volumes punctually (during GW events) and locally (above the Peninsula), as shown here. NAT PSC reach much larger volumes (green line in Figure 11), but are also locally dependent. The local maximum NAT volume (∼150 km^3/profile) is much larger than the average, in calm periods (28.4 km^3) and GW events (70.3 km^3). The maximum is East of the Peninsula (∼35°W), which suggests these NAT PSC form primarily through mountain-wave seeding triggered by ice PSC upstream. The seeding effect on NAT PSC volume starts

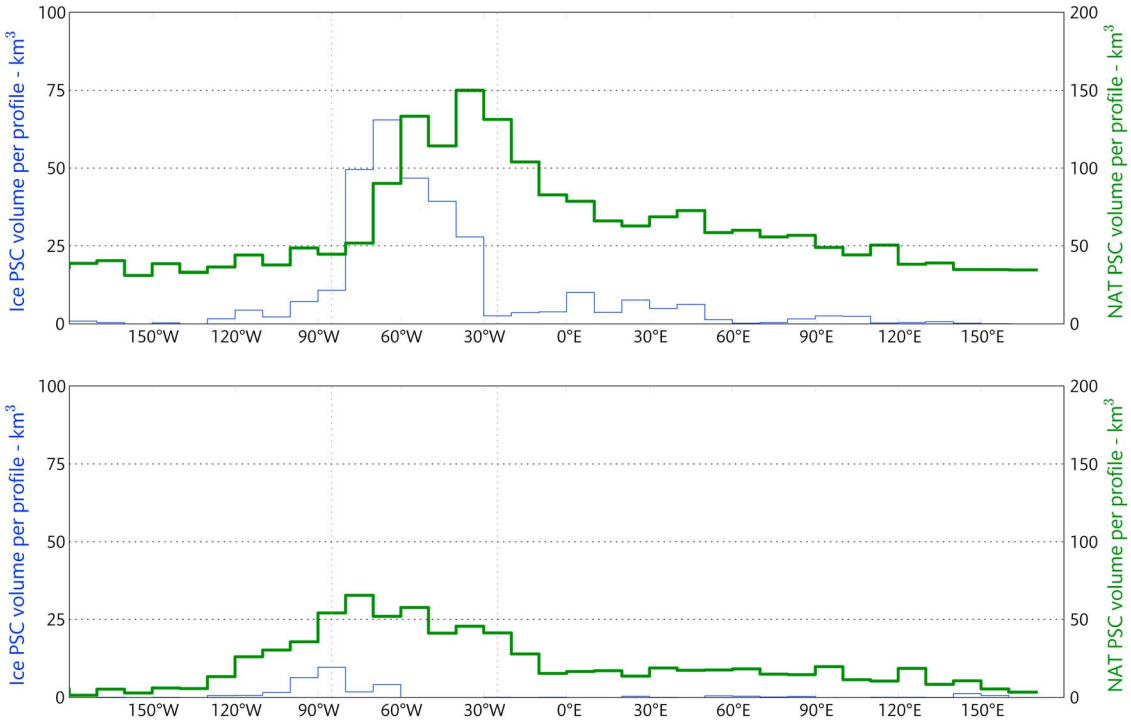

Figure 11. Volume of ice (blue, thin) and NAT (green, thick) PSC during (top) GW events and (bottom) calm periods, averaged per profile, as a function of longitude in 10° bins. Note that the range of the vertical axis for NAT PSC volume is double the one for ice PSC.

near 65°W, and extends as far as 40°E. GW-generated ice PSC therefore affect NAT PSC on several thousand kilometers, as found in *Alexander et al.* [2011]. The NAT PSC volume is minimum (~40 km^3) between 120°E and 120°W. This is larger than the average volume in GW-free periods, for reasons which will be discussed in section 4. Figure 11 shows no noticeable influence from GW activity happening over the TransAntarctic mountains, which would potentially lead to changes in PSC cover near 180°–150°W. A refined PSC classification scheme identifying Mix2-enh NAT PSC (identified using the optical properties retrieved by CALIOP as in *Pitts et al.* [2011]) shows that during GW events, they represent on average 38% of NAT PSC, up to 50% right over the Peninsula and a second maximum in the 50°E–100°E range (not shown).

[31] During calm periods (Figure 11, bottom), ice PSC almost disappear, as in section 3.4 (Figure 9). A few PSC still appear near 100°W–80°W, quite far upwind of the Peninsula. They form a geographically consistent cluster and cannot be attributed to data noise; we lack an explanation for their rather puzzling presence at this point. They could be created through GW activity west of the Peninsula that would lie outside the modeled domain and not be identified by the present analysis. By contrast, a background level of NAT PSC fluctuates between 50 km^3 above the Peninsula to ~20 km^3 East of 20°W. This is close to the average volume in calm periods (section 3.4) and to the volume 48 h after the end of GW events (section 3.5). Even during calm periods (unaffected by GW temperature fluctuations), volumes of NAT PSC fluctuate with longitude and are larger between 80°W and 20°W. This could be due to weak GW activity creating limited atmospheric perturbations above the Peninsula. These would not be identified as GW events, as they would fail to cross the 1 m/s wind speed threshold, but could still manage to cool temperatures below the NAT frost point (easier to reach than the ice frost point). During calm periods, Mix2-enh NAT PSC represent on average 30% of NAT PSC. This confirms the link between wave ice clouds and Mix2-enh particle types pointed out in *Pitts et al.* [2011], although 62% of NAT PSC are not Mix2-enh during GW.

[32] The two vertical dotted lines on Figure 11 limit the modeled domain used to identify GW (section 2). Figure 11 suggests that comparing model output with observations in that domain, as in the next section, should capture well enough the main effects of gravity waves on PSC, although some information (mostly about NAT PSC) might be lost East.

4. GW Activity, Frost Points and PSC

[33] Sections 2 and 3 document effects of gravity waves on PSC seen by CALIOP, thus adding to the significant evidence from literature. However, trying to quantify these effects raises two problems: (1) GW affect PSC formation when (and only when) they help to bring temperatures below the frost points. Even strong GW have zero impact if they fail to bring temperatures down enough, or if the stratosphere was already cold enough to begin with. This explains why GW events do not always affect PSC volumes (Figure 8, section 3.3). (2) Large-scale planetary waves drive pre-existing atmospheric conditions and the probability of PSC formation. When such waves

are advected by the polar vortex, their effects will interact with those of any present GW. This is apparent on Hovmoller diagrams in *Alexander et al.* [2011], where increased NAT PSC volumes above the Peninsula (linked to GW), propagating eastward (downwind), are part of larger NAT PSC systems originating west of the Peninsula (upwind) linked to planetary wave activity.

[34] These two effects, combined, make it very difficult to isolate and quantify the impact of gravity waves and mountain-wave seeding on PSC. In an attempt to work around these problems, in this section we relate observed ice and NAT PSC volumes to volumes colder than the frost points. Assuming the nucleation of PSC particles occurs homogeneously, this relation should be independent of changes in stratospheric conditions (temperature, pressure, concentrations). Changes in this relation could identify a qualitative change in the PSC particle formation process, such as the triggering of heterogeneous nucleation through the seeding effect.

4.1. Ice and NAT Frost Points

[35] Frost points were retrieved using observations from the Microwave Limb Sounder (MLS). Onboard Aura in the A-Train constellation, it is well colocated with CALIOP, especially at the Poles where the orbital shift between the two satellites is minimal. MLS vertical profiles of mixing ratios for water vapor and HNO_3 (Level 2 data v3.3, H2O and HNO3 products) were averaged daily over the considered domain (section 1.1). Profiles with Quality flag below 0.9 (for H_2O) and 0.4 (for HNO_3) were removed to avoid observations affected by tropospheric clouds [*Livesey et al.*, 2011]. Since the formation of PSC decreases gas phase HNO_3 and H_2O, their presence can bias MLS measurements and underestimate the actual abundance of either species. This would give a cold bias to our retrieved frost points [*Schoeberl et al.*, 2006]. To avoid this, MLS profiles were discarded if colocated CALIOP profiles (aggregated in a 180 km radius from the same A-Train overpass) revealed an average PSC thickness greater than 500 m per profile. MLS profiles with less than 4 colocated CALIOP profiles were also discarded since their corresponding PSC cover could not be retrieved. For water vapor, averaging was performed on $\log(H_2O)$ as recommended by the MLS documentation [see also *Vömel et al.*, 2007].

[36] In the 10–120 hPa range under study, the minimum MLS concentrations are 0.1 ppmv (H_2O) and 0.7 ppbv (HNO_3), and the resolutions ~3.5 km vertically, 200–400 km along-track and 7–10 km cross-track. Figure 12 shows mixing ratios of water vapor and HNO_3 from MLS measurements above the Peninsula for all years. In 2006, during a strong drying event between July 24th and August 8th, water vapor concentrations between 10 and 40 hPa fall from ~5 to 1.5 ppmv (top left). This event is characteristic of the wintertime Antarctic stratosphere [e.g., *Randel et al.*, 2004] and is more or less visible in all winter seasons (left column). A similar decrease is observed in HNO_3 mixing ratios (right column), but significant drops appear much earlier, during June. While the levels of stratospheric water vapor seem to stay constant from one year to the next, HNO_3 loading seem to increase from 2006 to 2010, when the seasonal decrease becomes almost inexistent. Both mixing ratios and the timing of the stratospheric drying agree with *Nedoluha et al.* [2002].

[37] Ice and NAT frost points were calculated as a function of time and altitude by applying the formulas of *Hanson and Mauersberger* [1988] and *Murphy and Koop* [2005] to daily averaged mixing ratio profiles (as in Figure 12) and full-resolution pressure and temperature fields from WRF. Figure 13 shows ice and NAT frost points retrieved from the mixing ratios shown in Figure 12 and simulations. Ice frost points (Figure 13, left) are stratified and decrease regularly with increasing altitude, from ~192 K at 100 hPa to ~183 K at 10 hPa. The drying event in the middle of the 2006 season translates to a 4 K frost point cooling (Figure 13, top left). It is mostly noticeable at 20 hPa but other levels are also affected. Other years are similarly affected depending on the intensity of the drying event. NAT frost points (Figure 13, right) evolve similarly, with a drop during the July–August transition, but are generally 5 to 7 K warmer (consistent with *Tabazadeh et al.* [1994]). In 2010, the NAT frost point cooling is almost inexistent, in sync with the HNO_3 levels (Figure 12, bottom right).

4.2. GW Activity and Volume Colder Than the Frost Points

[38] Here we compare ice and NAT frost points with WRF temperatures, to quantify the volume of stratospheric air able to sustain PSC formation.

[39] Table 3 shows volumes colder than ice and NAT frost points (V_{Tice} and V_{TNAT}, respectively), for each simulated year and on average for each month. The largest V_{Tice} are in 2010 and 2008, the smallest in 2007. V_{TNAT} are much more stable and similar cross years, there is a noticeable maximum in 2006. Over all years, the minimum V_{Tice} is observed in June and the maximum in August (when volumes are ~4 times as large). Volumes in September go back to June levels. This follows the seasonal stratospheric evolution, which gets globally colder as the austral winter progresses and gets warm again in September. V_{TNAT} follow the same monthly evolution (minimum in June, maximum in August), but the relative increase is much less dramatic (+25%) than for ice. These volumes should not be directly compared to the average PSC volumes found in section 3 (Table 1), as they document different domains (a valid comparison is conducted later in the section). They can however be compared with GW events described in Table 1. The absence of any clear correlation between cold volumes and GW properties (either their total length of events, the affected volume or the maximum wind speed) suggests that V_{Tice} and V_{TNAT} are most likely driven by large-scale synoptic changes, rather than by intense but small-scale fluctuations from GW. This is especially notable for September, which shows an intense GW activity (section 2.4) but limited V_{Tice}.

[40] Figure 14 shows the evolution of V_{Tice} during all studied Antarctic winters. GW events (identified with thick lines) generally correlate poorly to increases in V_{Tice}- large V_{Tice} are seen during non-GW periods. This is especially noticeable in 2009, when most of temperatures colder than the ice frost point are in August. August 2009 shows only limited GW activity, and its temperature is mostly driven by the large-scale stratospheric cooling of the winter season. Moreover, small V_{Tice} are seen during GW events. These remarks confirm that the impact of GW on frost point crossing is extremely dependent on the initial, pre-GW atmospheric conditions. However, GW events correlate

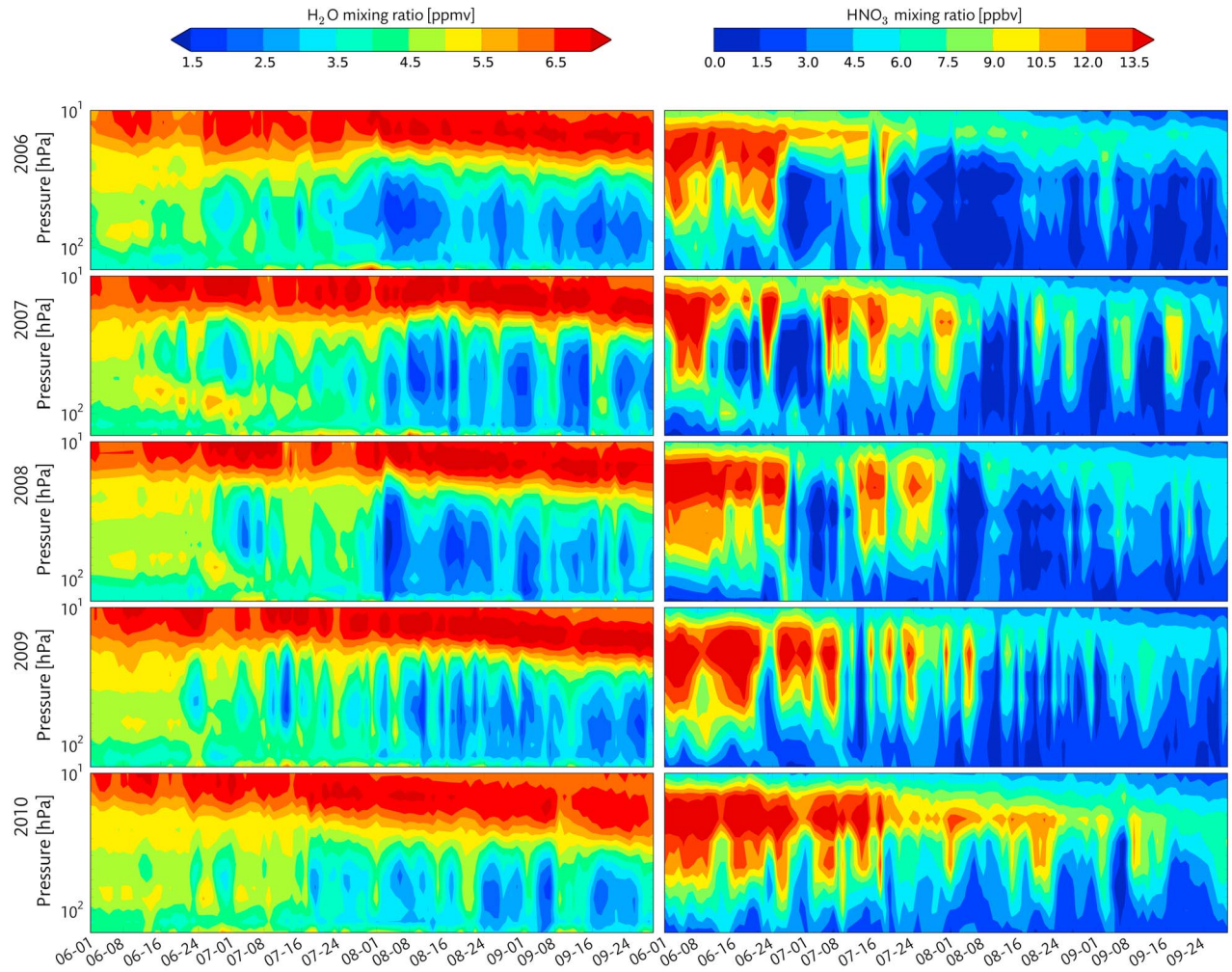

Figure 12. Time series of (left) water vapor mixing ratios and (right) HNO_3 profiles observed by MLS and averaged daily over the simulation domain for winter seasons between (top) 2006 and (bottom) 2010.

quite well with increases in V_{Tice} near the start of the season (see June and early July in 2006 and 2008). This supports the increased influence of GW early in the season for PSC formation.

[41] Figure 15 shows the distribution of daily V_{Tice}, during GW events days (left) or not (right) over the 2006–2010 period. GW-affected days show smaller V_{Tice}, but also larger ones, i.e., the distribution is broader. An explanation is that without GW, V_{Tice} is primarily driven by large-scale seasonal temperature change, meaning these volumes are either nonexistent (early winter, warm stratosphere) or large (late winter, cold stratosphere). When present, GW create small-scale temperature drops leading to lots of small V_{Tice} in periods warmer than the ice frost point (i.e., June). Later in the season (i.e., August), GW temperature drops provide a slight increase to the already-large V_{Tice}. These two effects combine to increase small and large V_{Tice} in GW events. Daily average V_{Tice} are slightly larger during non-GW days.

[42] Previous sections show that ice PSC are clearly much larger in GW events (section 3.4), and are almost nonexistent without GW. However, large volumes colder than the ice frost point appear both during and outside of GW events. The cooling ability of GW events therefore cannot be solely responsible for their influence on PSC formation: even if GW do impact stratospheric temperatures, they are not their main influence and are not necessary to drive them below the frost point in large volumes. Such temperatures are routinely reached in large volumes even during calm periods. It is possible the speed of the GW temperature drops, or their intensity, are responsible for the enhanced PSC formation.

4.3. PSC Volumes and Volumes Below Frost Points

[43] As noted previously, PSC volumes from CALIOP (section 3) cannot be compared directly to frost point volumes from WRF and MLS measurements (section 4.2). CALIOP's sampling is local and irregular in time, while the simulated domain is geographically restricted. Thus, to compare PSC observations and simulations, the following steps were followed: (1) for each CALIOP orbit overpassing the model domain, the closest simulation in time was identified. The worst-case time delta with observations is therefore 3 h (the simulation time step); (2) the output fields of the identified simulation were extracted along CALIOP's orbit coordinates and regridded on its altitude levels, respecting the simulated vertical pressure structure. In other words,

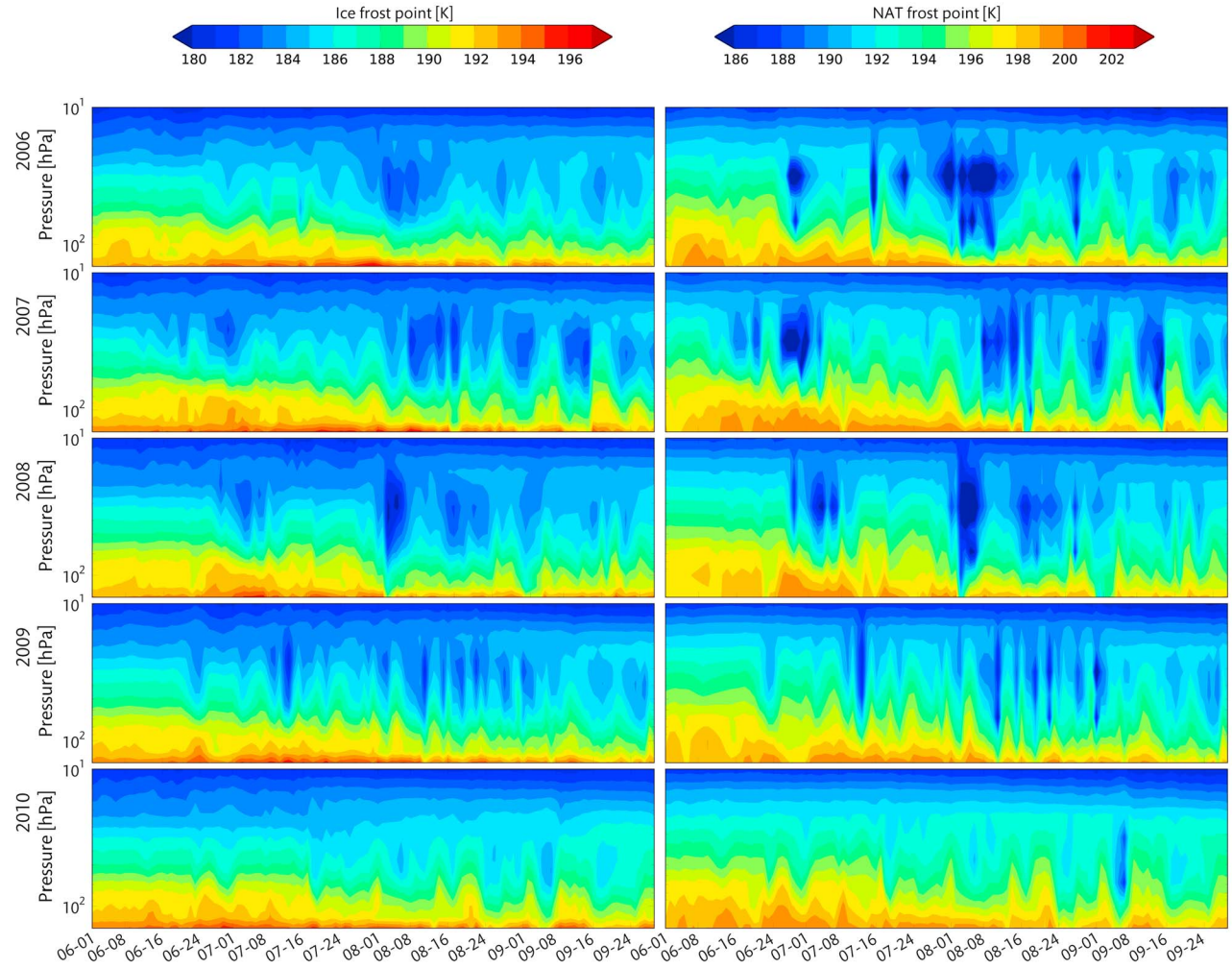

Figure 13. Same as Figure 12, for (left) ice and (right) NAT frost point profiles retrieved from the daily averaged MLS water vapor mixing ratios shown in Figure 12 and WRF simulation output.

simulated stratospheric fields were extracted at the time, location and altitude of CALIOP observations to produce a space-time intersection of observed PSC and simulated frost points volumes. These volumes, discussed in the rest of this section, do not describe the same areas and periods as those from sections 2 and 3. Information about GW activity is still relevant though, as it pertains to the simulation domain as a whole.

[44] Intersecting volumes of ice PSC and V_{Tice} are correlated. As an example, Figure 16 (top) shows their daily evolution for the 2006 Antarctic winter. Until August 8th, fluctuations in observed ice PSC volumes are consistent with V_{Tice}. Even if V_{Tice} are often larger, increases and decreases in both values appear correlated. The correlation breaks down after August 8th, when the ice PSC volume drops significantly, several days before a drop in cold volumes. These discrepancies are probably due to the fact that supersaturations near 1.6 (corresponding to a supercooling of ~3 K below the ice frost point) are required for freezing the STS particles into ice crystals [*Koop et al.*, 2000]. By contrast, the NAT PSC volume (Figure 16, bottom) is always much smaller than V_{TNAT}, and their daily fluctuations show no apparent correlation, except when HNO_3 levels drop abruptly and lead to a significant drop in NAT frost point (compare the period near July 1st in Figures 12, 13 and 16). This lack of immediate correlation is probably due to the slow nucleation of NAT particles, which requires air to stay colder than the NAT frost point for at least ~24 h [*Tabazadeh et al.*, 1996], but can evaporate much faster.

Table 3. Average Daily Volume With Temperatures Below the Ice and NAT Formation Temperature Thresholds T_{ice} and T_{NAT}, for Each Year Between 2006 and 2010 and Each Month[a]

	Daily Volume With $T < T_{ice}$ (10^6 km^3)	Daily Volume With $T < T_{NAT}$ (10^6 km^3)
2006	2.21	**19.1**
2007	2.19	16.7
2008	2.53	17.7
2009	2.43	17.4
2010	**3.33**	17.5
June	1.4	15.5
July	2.7	18.3
August	**4.3**	**20.3**
September	1.6	16.7

[a]Maximum volumes are boldface.

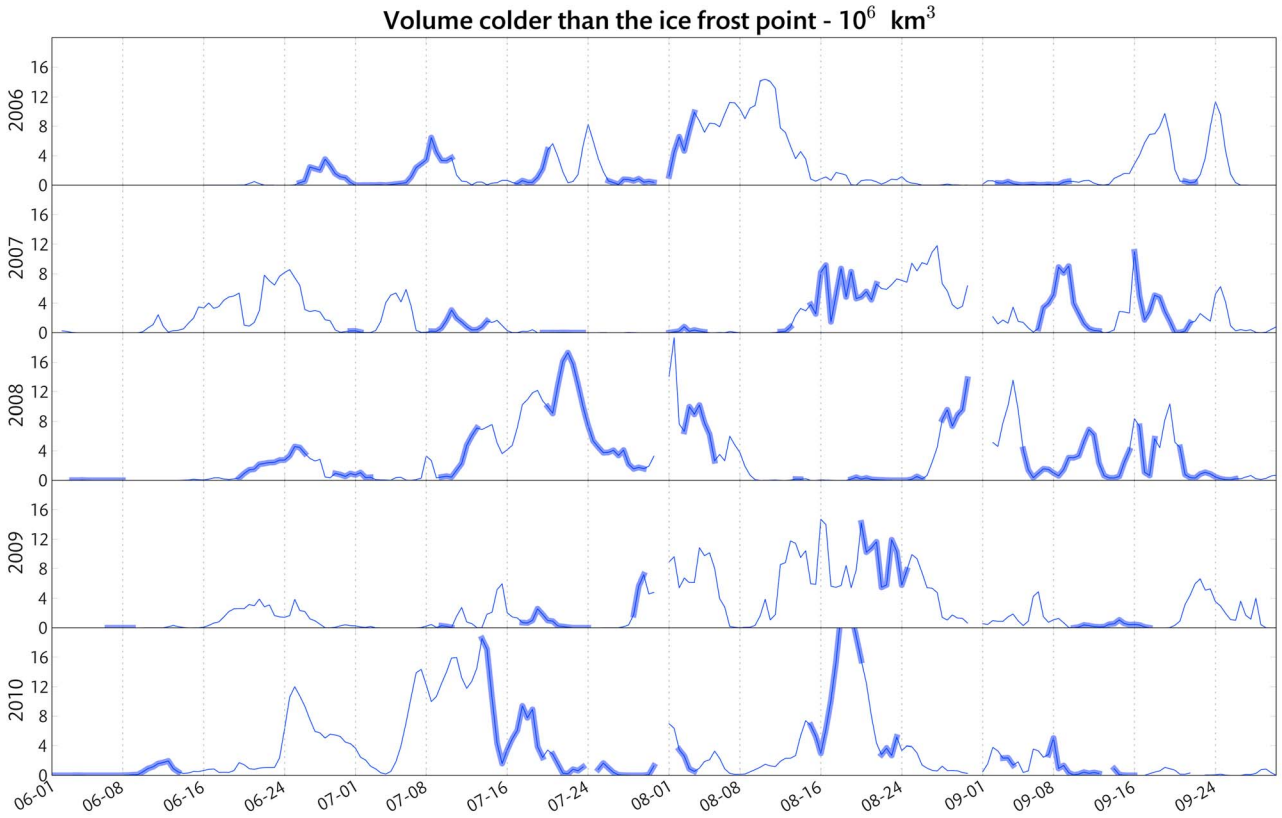

Figure 14. Evolution of daily domain volume colder than the ice frost point for Antarctic winters between (top to bottom) 2006 and 2010. GW events described in section 2 are identified by thick lines.

Here, GW temperature drops seem too fast to significantly affect the NAT PSC volume, and the formation of NAT PSC depends more on the synoptic background temperature than on the instantaneous local temperature. The fact that V_{TNAT} are much larger than NAT PSC volumes also suggests that the possible cold bias in NAT frost points (discussed in section 4.1) does not impact the present results significantly.

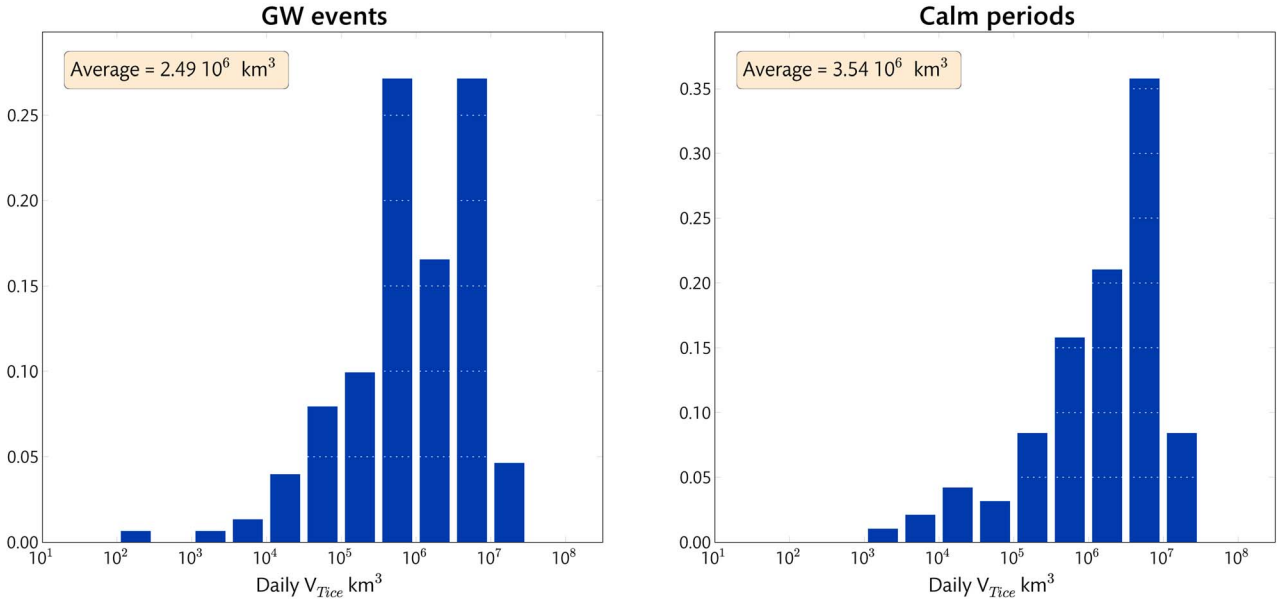

Figure 15. Distributions of daily volumes with temperatures colder than the ice frost point, during (left) GW events and (right) calm periods.

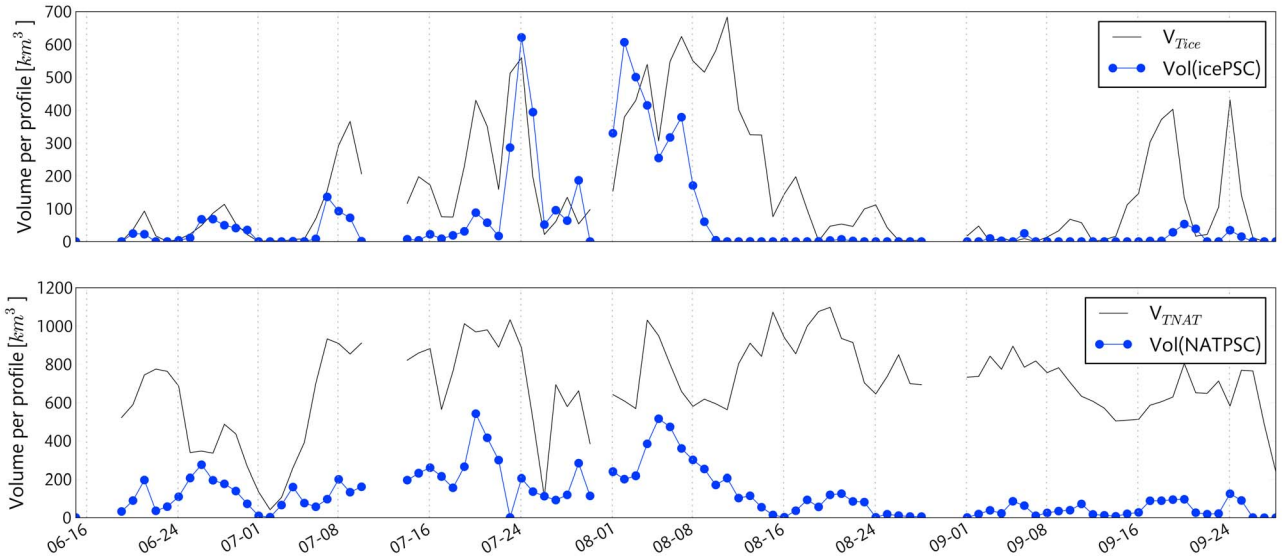

Figure 16. Simultaneous evolution during the 2006 Antarctic winter of volumes with stratospheric temperatures below the frost point (line) and volumes of PSC (dots), for (top) ice and (bottom) NAT particles using the intersection of WRF model output with CALIOP observations.

[45] Figure 17 shows the distribution of colocated and simultaneous ice PSC volumes and V_{Tice} in individual profiles (no averaging) for the entire studied data set (2006–2010). As with the daily averages (Figure 16), instantaneous profile values are highly correlated (correlation coefficient ~0.52, average ratio between both 0.94). Agreement seems best in profiles with large volumes. This linear correlation is not found between volumes of NAT PSC and V_{TNAT} (not shown). The average ratio between both volumes is close to 0.42. Again, this is not surprising given the slower nucleation of NAT crystals. These results show that temperature drops have a strong visible impact on ice PSC, but not on NAT PSC. Since the observed NAT PSC cover is considerably larger during GW events (section 3), an external mechanism must be responsible, such as mountain-wave seeding.

4.4. Ratios of PSC Volumes on Volumes Colder Than the Frost Point

[46] From here on, ratios of PSC volumes on volumes colder than the relevant frost point shall be referred to as ice ratio (ice PSC volume on V_{Tice}) and NAT ratio (NAT PSC volume on V_{TNAT}). These ratios describe PSC nucleation

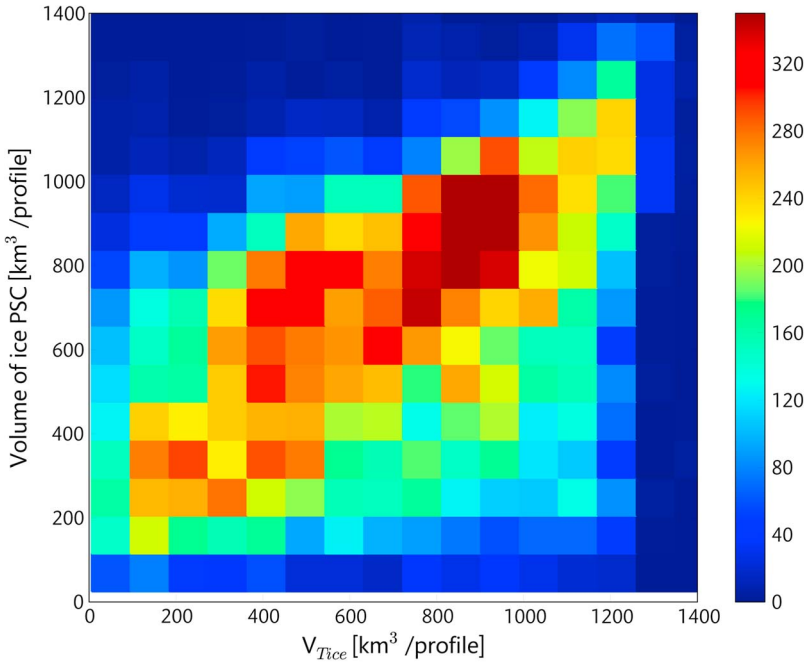

Figure 17. Histogram of observed ice PSC volume versus volumes colder than the ice frost point.

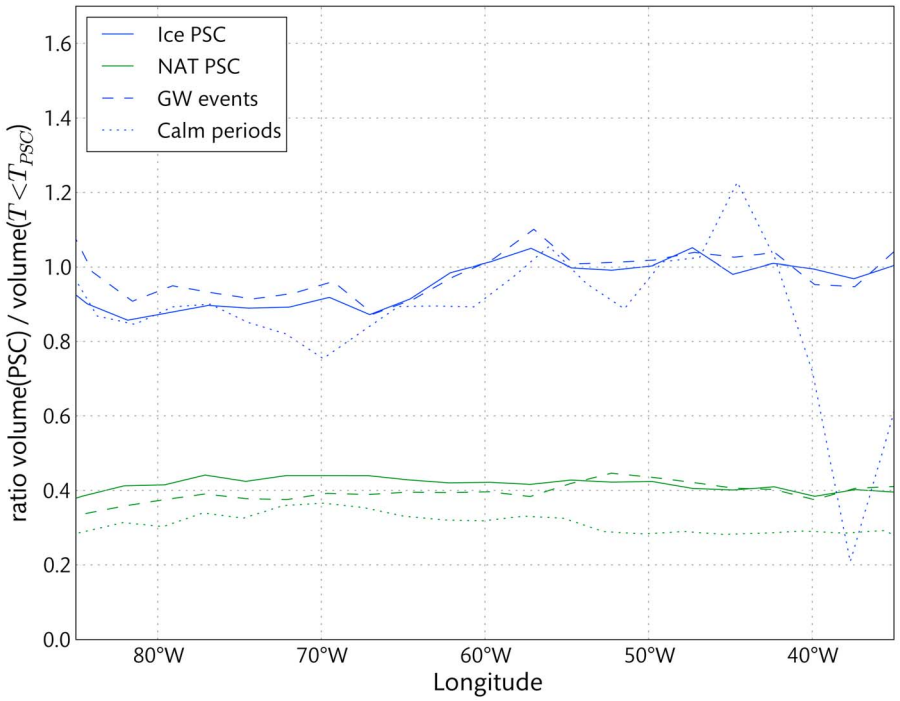

Figure 18. Ratio of the observed volume of PSC on the modeled volume colder than its respective frost point, for ice PSC (blue) and NAT PSC (green), considering all periods (full line), GW events (dashed lines) and calm periods (dotted lines).

efficiency, and thus should diagnose the impact of external factors on PSC formation, independently of stratospheric temperature or mixing ratios. Figure 18 shows the evolution of the ice and NAT ratios as a function of longitude, for the entire period (full lines), during GW events (dashed lines) and calm periods (dotted lines). The ice ratio (blue lines) oscillates around 1, consistently with the behavior observed in Figure 17: the ice PSC volume is approximately equal to V_{Tice}. Ice ratios are however lower west of 60°W and greater east, a tendency that slightly intensifies East during GW events. Values are mostly similar during calm periods, although values are noisier since V_{Tice} is very limited outside of GW events. The NAT ratio (green lines) also stays approximately constant with longitude, and stays in the 0.4–0.5 range. During GW events, the NAT ratio is slightly smaller than average west of 55°W and greater east. Enhanced NAT ratios (East of 55°W) appear East of enhanced ice ratios, consistent with NAT formation downstream from the Peninsula. The NAT ratio is weaker during calm periods, which is consistent with an increased nucleation efficiency during GW events. NAT ratios are also weaker in June and September (0.2–0.3) compared to the July–August period (0.4–0.5).

[47] Near-unity ice ratios (Figures 17 and 18) are consistent with a fast formation of crystals. Water vapor reacts fast to temperature drops, either slow from synoptic-scale atmospheric changes or fast from local fluctuations caused by gravity waves. As a consequence, there is an almost one-to-one correspondence between simulated V_{Tice} and observed volumes of ice PSC. Ice ratios greater than 1, as observed eastward of the Peninsula, can either be due to (1) the model underestimating V_{Tice}, in which case they would be nongeophysical (a very likely possibility, given the WRF warm bias compared to radiosonde measurements found in section 2.5); (2) important sedimentation of crystals below the areas colder than the ice frost point, which would survive long enough to be observed by CALIOP and identified as ice PSC before they sublimate; (3) a slowed down evaporation process due to NAT surface coating (as *Peter et al.* [1994] proposed to explain in situ observations in leewave PSC). These possibilities would allow the volume of observed ice PSC to get larger than the volume of temperatures able to sustain them. Both possibilities would get worse during GW, which is consistent with the results. The absence of significant change in NAT ratio during GW events apparently contradicts the mountain-wave seeding effect. This effect should lead ice PSC to trigger an accelerated formation of NAT crystals. This should record as a clear NAT ratio increase, which is absent in Figure 18. There is an increase east of 55°E, but extremely weak, and smaller than the ice ratio increase east of 60°W which is potentially due to uncertainties in model output. The observed fluctuations of NAT ratio therefore cannot be reliably considered physically meaningful.

[48] Figure 19 shows the NAT ratio function of the delay after a given volume of ice PSC was observed. After no or little ice PSC are observed (<15 km^3 per profile), the NAT ratio stays more or less constant with time (dashed line) between 0.2 and 0.25. After large volumes of ice PSC are observed (full lines), the NAT ratio starts increasing rapidly, and stays above 0.25 two to six hours later. This translates to a 50–100% increase in NAT PSC formation efficiency above average. Afterwards, the NAT ratio decreases slowly, reaching 0.1 twenty hours after ice PSC observation (less

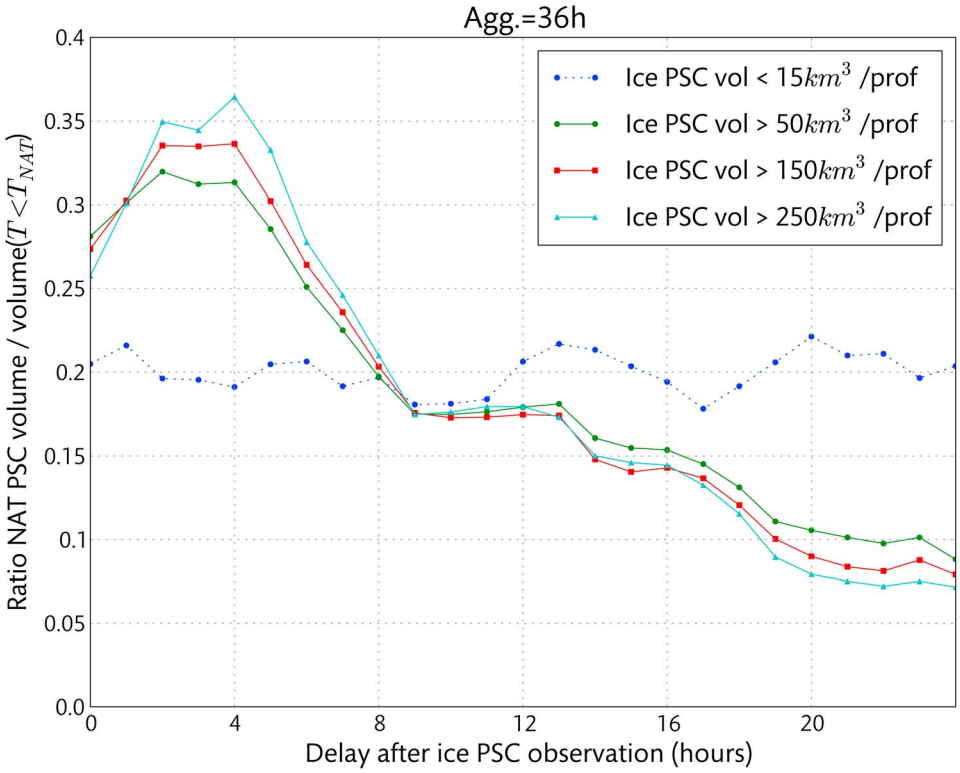

Figure 19. Ratio of the observed volume of NAT PSC on the modeled volume colder than the NAT frost point, for four ranges of observed ice PSC volumes, as a function of the delay after ice PSC observation. Volumes were aggregated over 36 h periods with an adjustable delay between ice and NAT data.

than 50% of the average NAT PSC formation efficiency). The intensity of the initial increase and its following drop depends on the volume of ice PSC observed: larger volumes lead to a stronger increase in NAT ratio (more than 0.4 for volumes greater than 250 km^3/profile), followed by a stronger drop (down to 0.07). We suggest the strong initial increase in NAT PSC formation efficiency is due to the use of crystals from ice PSC as nucleation seeds leading to an efficient transformation of available HNO_3 into NAT crystals. This is supported by the correlation between volumes of ice PSC and increases in NAT ratio - larger ice PSC mean more crystals available for NAT nucleation. The below-average NAT ratios in the following hours might be due to the mountain-wave generated NAT crystals sublimating and going back to HNO_3 form. This explains why no effect from GW appears when showing the NAT ratio as a function of longitude (Figure 17), as these two effects cancel each other out, leading to zero effect on average.

5. Discussion

[49] This article compares mesoscale simulations of stratospheric conditions with volumes of PSC observed by spaceborne lidar above the Antarctic Peninsula, to better understand how Gravity Waves affect their formation and properties.

[50] Simulated vertical winds were analyzed to identify intense and long-lived GW events (section 2) above the Antarctic Peninsula during five Antarctic winters (2006–2010). Main results involve the documentation of GW activity in this domain and period, including daily fluctuations of fastest winds and coldest temperatures. We present a calendar of GW events, and the geographic distribution of GW activity over the studied area. GW activity was especially strong in 2006 and 2008, and weak in 2009. GW affect ~36% of days and are generally stronger in July and weaker in August. Maximum GW activity is right above the high mountain of the Peninsula, with a second, much weaker maximum above the Douglas Range on Alexander Island. June and September shows intense GW, with large fractions of the domain affected by fast vertical winds. In these warmest months of the season, GW activity has the most noticeable impact on PSC formation. A consistent warm bias of 1.3 K was found in stratospheric temperatures compared to radiosonde measurements, unrelated to GW activity.

[51] We then correlated observations of ice and NAT PSC over Antarctica with GW activity, to investigate their potential effect on PSC properties (section 3). We document the evolution and distribution of daily ice and NAT PSC volumes during GW events and calm periods. Even though GW only affect ~36% of days, 63% of ice PSC volume were observed during GW events. Volume of ice PSC doubled during GW events, reaching 20 km^3/profile. Since GW activity is unrelated to seasonal cooling, this change in ice PSC volume is not due to large-scale temperature changes, and is related to GW activity instead. On the other hand, 46% of NAT PSC were observed during GW event. This suggests the effect of GW on these clouds is weaker, yet significant. Our results are consistent with *Alexander et al.* [2011], who found ~50% of ice and NAT PSC were due

to GW during 2007. Years with long GW events show larger NAT PSC volumes, and years with short events larger ice PSC volumes. This suggests the length of events, and more generally timing issues, influence how GW events affect PSC. Volumes of ice PSC are strongly longitude-dependent and are largest above the Peninsula (∼65°W), while volumes of NAT PSC are largest near ∼35°W, far downstream with respect to the polar vortex. We showed that after a GW event, ice PSC volumes get back to the near-zero volumes of calm periods in 12 to 24 h, with a steep decline during the first 12 h. Volumes of NAT PSC take as long as 48 h to get back to non-GW levels. These results strongly support the importance of mountain-wave seeding for NAT PSC formation above Antarctica. The impact of this mechanism is felt as far East as 40°E, several thousand kilometers downstream of GW activity.

[52] Finally, we analyzed the intersection of observations with model output, combined with water vapor and HNO_3 mixing ratios observed from space, to investigate changes in PSC formation efficiency due to gravity waves (section 4). We documented volumes colder than ice and NAT frost points above the Peninsula, information important for studies of stratospheric clouds. We showed that daily and instantaneous volumes of ice PSC are closely correlated with volumes colder than the ice frost point, irrespectively of GW events. Large volumes colder than the ice frost points are observed even without GW, thus the ability of GW to bring temperatures down is not solely responsible for the increased ice PSC observed during them. It could be possible that the speed and intensity of GW temperature drops plays a role in the enhanced ice PSC formation, but this hypothesis needs to be tested. While drops in V_{TNAT} due to decreasing HNO_3 levels correlates well with a decrease in NAT PSC volumes, such a correlation is not observed when V_{TNAT} increases. This is explained by the slower nucleation of NAT crystals. Finally, the observation of ice PSC leads to a strong increase (+50–100%) in NAT PSC formation efficiency 2 to 6 h later. This increase can be attributed to enhanced NAT crystal nucleation, using ice crystals as seeds. It is followed by a sharp drop 6 h to 10 h after ice PSC observation, and a longer slow decline (10 h–24 h), that we attribute to sublimation of the mountain wave-generated NAT PSC. After this period, NAT PSC formation efficiency is less than half its initial value. The amplitude of the initial increase and following decline in NAT PSC formation efficiency depends on the volume of ice crystals available as NAT nucleation seeds.

[53] Among other things, our results show that (1) after the end of GW events, NAT PSC volumes take up to 48 h to go back to non-GW levels; (2) during GW events, a short period of increased NAT formation efficiency is followed by a long decline to lower efficiency levels. The influence of these two phenomena, which imply significant delays in mountain-wave seeding, might explain why it is difficult to quantitatively correlate GW activity to changes in NAT PSC volumes.

[54] **Acknowledgments.** The authors would like to thank the IPSL ClimServ center for computational facilities and storage, the ICARE Data Center and the NASA Atmospheric Sciences Data Center for CALIOP and MLS data availability, as well as A. Hertzog for article review. We would like to thank the anonymous reviewers for several suggestions that significantly improved the paper. Rothera Antarctic High Resolution Radiosonde Data were provided by NCAS British Atmospheric Data Centre, available from http://badc.nerc.ac.uk/view/badc.nerc.ac.uk__ATOM__dataent_12220884243426614.

References

Alexander, M. J., and H. Teitelbaum (2007), Observation and analysis of a large amplitude mountain wave event over the Antarctic Peninsula, *J. Geophys. Res.*, *112*, D21103, doi:10.1029/2006JD008368.

Alexander, S. P., A. R. Klekociuk, and T. Tsuda (2009), Gravity wave and orographic wave activity observed during the Antarctic and Arctic stratospheric vortices by the COSMIC GPS-RO satellite constellation, *J. Geophys. Res.*, *114*, D17103, doi:10.1029/2009JD011851.

Alexander, S. P., A. R. Klekociuk, M. C. Pitts, A. J. McDonald, and A. Arevalo-Torres (2011), The effect of orographic gravity waves on Antarctic Polar Stratospheric Cloud (PSC) occurrence and composition, *J. Geophys. Res.*, *116*, D06109, doi:10.1029/2010JD015184.

Baumgaertner, A. J. G., and A. J. McDonald (2007), A gravity wave climatology for Antarctica compiled from Challenging Minisatellite Payload/Global Positioning System (CHAMP/GPS) radio occultations, *J. Geophys. Res.*, *112*, D05103, doi:10.1029/2006JD007504.

Carslaw, K. S., et al. (1998), Particle microphysics and chemistry in remotely observed mountain polar stratospheric clouds, *J. Geophys. Res.*, *103*, 5785–5796, doi:10.1029/97JD03626.

Connolley, W. M., and J. C. King (1993), Atmospheric water-vapour transport to Antarctica inferred from radiosonde data, *Q. J. R. Meteorol. Soc.*, *119*, 325–342, doi:10.1002/qj.49711951006.

Fueglistaler, S., et al. (2002), Large NAT particle formation by mother clouds: Analysis of SOLVE/THESEO-2000 observations, *Geophys. Res. Lett.*, *29*(12), 1610, doi:10.1029/2001GL014548.

Hanson, D., and K. Mauersberger (1988), Laboratory studies of the nitric acid trihydrate: Implications for the south polar stratosphere, *Geophys. Res. Lett.*, *15*(8), 855–858, doi:10.1029/GL015i008p00855.

Hitchcock, P., T. G. Shepherd, and C. McLandress (2009), Past and future conditions for polar stratospheric cloud formation simulated by the Canadian Middle Atmosphere Model, *Atmos. Chem. Phys.*, *9*(2), 483–495, doi:10.5194/acp-9-483-2009.

Höpfner, M., et al. (2006), MIPAS detects Antarctic stratospheric belt of NAT PSCs caused by mountain waves, *Atmos. Chem. Phys.*, *6*, 1221–1230, doi:10.5194/acp-6-1221-2006.

Höpfner, M., M. C. Pitts, and L. R. Poole (2009), Comparison between CALIPSO and MIPAS observations of polar stratospheric clouds, *J. Geophys. Res.*, *114*, D00H05, doi:10.1029/2009JD012114.

Innis, J., and A. Klekociuk (2006), Planetary wave and gravity wave influence on the occurrence of polar stratospheric clouds over Davis Station, Antarctica, seen in lidar and radiosonde observations, *J. Geophys. Res.*, *111*, D22102, doi:10.1029/2006JD007629.

Jensen, E. J., O. Toon, A. Tabazadeh, and K. Drdla (2002), Impact of polar stratospheric cloud particle composition, number density, and lifetime on denitrification, *J. Geophys. Res.*, *107*(D20), 8284, doi:10.1029/2001JD000440.

Kohma, M., and K. Sato (2011), The effects of atmospheric waves on the amounts of polar stratospheric clouds, *Atmos. Chem. Phys.*, *11*(22), 11,535–11,552, doi:10.5194/acp-11-11535-2011.

Koop, T., B. P. Luo, A. Tsias, and T. Peter (2000), Water activity as the determinant for homogeneous ice nucleation in aqueous solutions, *Nature*, *406*, 611–614, doi:10.1038/35020537.

Livesey, N. J., et al. (2011), Aura Microwave Limb Sounder (MLS) version 3.3 level 2 data quality and description document, version 3.3 × −1.0, *JPL D-33509*, 162 pp., Jet Propul. Lab., Pasadena, Calif. [Available at http://mls.jpl.nasa.gov/data/v3-3_data_quality_document.pdf.]

Marti, J., and K. Mauersberger (1993), A survey and new measurements of ice vapor pressure at temperatures between 170 and 250 K, *Geophys. Res. Lett.*, *20*(5), 363–366, doi:10.1029/93GL00105.

Martins, E., V. Noel, and H. Chepfer (2011), Properties of cirrus and subvisible cirrus from nighttime Cloud-Aerosol Lidar with Orthogonal Polarization (CALIOP), related to atmospheric dynamics and water vapor, *J. Geophys. Res.*, *116*, D02208, doi:10.1029/2010JD014519.

McDonald, A., S. George, and R. Woollands (2009), Can gravity waves significantly impact PSC occurrence in the Antarctic?, *Atmos. Chem. Phys.*, *9*, 8825–8840, doi:10.5194/acp-9-8825-2009.

Moffat-Griffin, T., R. E. Hibbins, M. J. Jarvis, and S. R. Colwell (2011), Seasonal variations of gravity wave activity in the lower stratosphere over an Antarctic Peninsula station, *J. Geophys. Res.*, *116*, D14111, doi:10.1029/2010JD015349.

Murphy, D. M., and T. Koop (2005), Review of the vapour pressures of ice and supercooled water for atmospheric applications, *Q. J. R. Meteorol. Soc.*, *131*, 1539–1565, doi:10.1256/qj.04.94.

Nedoluha, G. E., R. M. Bevilacqua, and K. W. Hoppel (2002), POAM III measurements of dehydration in the Antarctic and comparisons with the Arctic, *J. Geophys. Res.*, *107*(D20), 8290, doi:10.1029/2001JD001184.

Noel, V., A. Hertzog, H. Chepfer, and D. Winker (2008), Polar stratospheric clouds over Antarctica from the CALIPSO spaceborne lidar, *J. Geophys. Res.*, *113*, D02205, doi:10.1029/2007JD008616.

Noel, V., A. Hertzog, and H. Chepfer (2009), CALIPSO observations of wave-induced PSCs with near-unity optical depth over Antarctica in 2006–2007, *J. Geophys. Res.*, *114*, D05202, doi:10.1029/2008JD010604.

Peter, T., R. Müller, P. J. Crutzen, and T. Deshler (1994), The lifetime of leewave-induced ice particles in the Arctic stratosphere: II. Stabilization due to NAT-coating, *Geophys. Res. Lett.*, *21*(13), 1331–1334, doi:10.1029/93GL03019.

Pitts, M. C., L. W. Thomason, L. R. Poole, and D. M. Winker (2007), Characterization of polar stratospheric clouds with spaceborne lidar: CALIPSO and the 2006 Antarctic season, *Atmos. Chem. Phys.*, *7*(19), 5207–5228, doi:10.5194/acp-7-5207-2007.

Pitts, M. C., L. R. Poole, and L. W. Thomason (2009), CALIPSO polar stratospheric cloud observations: Second-generation detection algorithm and composition discrimination, *Atmos. Chem. Phys.*, *9*, 7577–7589, doi:10.5194/acp-9-7577-2009.

Pitts, M. C., L. R. Poole, A. Dornbrack, and L. W. Thomason (2011), The 2009–2010 Arctic polar stratospheric cloud season: A CALIPSO perspective, *Atmos. Chem. Phys.*, *11*(5), 2161–2177, doi:10.5194/acp-11-2161-2011.

Plougonven, R., A. Hertzog, and H. Teitelbaum (2008), Observations and simulations of a large-amplitude mountain wave breaking over the Antarctic Peninsula, *J. Geophys. Res.*, *113*, D16113, doi:10.1029/2007JD009739.

Poole, L. R., and P. McCormick (1988), Airborne lidar observations of arctic polar stratospheric clouds: Indications of two distinct growth stages, *Geophys. Res. Lett.*, *15*, 21–23, doi:10.1029/GL015i001p00021.

Randel, W., F. Wu, O. S. J. Oltmans, K. Rosenlof, and G. E. Nedoluha (2004), Interannual changes of stratospheric water vapour and correlations with tropical tropopause temperatures, *J. Atmos. Sci.*, *61*, 2133–2148, doi:10.1175/1520-0469(2004)061<2133:ICOSWV>2.0.CO;2.

Schoeberl, M. R., et al. (2006), Chemical observations of a polar vortex intrusion, *J. Geophys. Res.*, *111*, D20306, doi:10.1029/2006JD007134.

Simmons, A., S. Uppala, D. Dee, and S. Kobayashi (2006), ERA-Interim: New ECMWF reanalysis products from 1989 onwards, *ECMWF Newsl.*, *110*, 25–35.

Skamarock, W. C., J. B. Klemp, J. Dudhia, D. O. Gill, D. M. Barker, W. Wang, and J. G. Powers (2005), A description of the advanced research WRF version 2, *NCAR/TN–468+STR*, 100 pp., NCAR, Boulder, Colo.

Solomon, S. (1999), Stratospheric ozone depletion: A review of concepts and history, *Rev. Geophys.*, *37*(3), 275–316, doi:10.1029/1999RG900008.

Steinbrecht, W., H. Claude, F. Schönenborn, U. Leiterer, H. Dier, and E. Lanzinger (2008), Pressure and temperature differences between Vaisala RS80 and RS92 radiosonde systems, *J. Atmos. Oceanic Technol.*, *25*(6), 909–927, doi:10.1175/2007JTECHA999.1.

Tabazadeh, A., R. P. Turco, K. Drdla, M. Z. Jacobson, and O. B. Toon (1994), A study of Type I polar stratospheric cloud formation, *Geophys. Res. Lett.*, *21*(15), 1619–1622, doi:10.1029/94GL01368.

Tabazadeh, A., O. B. Toon, B. L. Gary, J. T. Bacmeister, and M. R. Schoeberl (1996), Observational constraints on the formation of Type Ia polar stratospheric clouds, *Geophys. Res. Lett.*, *23*(16), 2109–2112, doi:10.1029/96GL01998.

Tsias, A., et al. (1999), Aircraft lidar observations of an enhanced type Ia polar stratospheric clouds during APE-POLECAT, *J. Geophys. Res.*, *104*(D19), 23,961–23,969, doi:10.1029/1998JD100055.

Vömel, H., et al. (2007), Validation of Aura Microwave Limb Sounder water vapor by balloon-borne cryogenic frost point hygrometer measurements, *J. Geophys. Res.*, *112*, D24S37, doi:10.1029/2007JD008698.

Winker, D., W. Hunt, and M. McGill (2007), Initial performance assessment of CALIOP, *Geophys. Res. Lett.*, *34*, L19803, doi:10.1029/2007GL030135.